Bright luminescent optically engineered core/alloyed shell quantum dots : an ultrasensitive signal transducer for dengue virus RNA via localized surface plasmon resonance-induced hairpin hybridization

Bright luminescent optically engineered core/alloyed shell quantum dots: An ultrasensitive signal transducer for dengue virus RNA via localized surface plasmon resonance-induced hairpin hybridization†

Oluwasesan Adegoke,[a] Enoch Y. Park[*,a,b]

[a] *Laboratory of Biotechnology, Research Institute of Green Science and Technology, Shizuoka University, 836 Ohya, Suruga-ku, Shizuoka 422-8529, Japan*
E-mail: adegoke.sesan@mailbox.co.za, park.enoch@shizuoka.ac.jp

[b] *Laboratory of Biotechnology, Department of Bioscience, Graduate School of Science and Technology, Shizuoka University, 836 Ohya, Suruga-ku, Shizuoka 422-8529, Japan*

† Electronic supplementary information (ESI) available: MTT viability assay of Qdot606 to HEK 293T cells, PL lifetime decay curves of the Qdots, TEM images of the Qdot-AuNP-MB biosensor conjugates, DLS and zeta potentials of the Qdot-AuNP nanohybrids, DLS and zeta potential curves for the Qdot-AuNP-MB biosensor conjugates, fluorescence quenching effects of the L-cysteine AuNPs on the Qdots after conjugation and the fluorescence quenching effects of the MB on the Qdot-AuNP conjugates.

[*] Laboratory of Biotechnology, Research Institute of Green Science and Technology, Shizuoka University, 836 Ohya, Suruga-ku, Shizuoka 422-8529, Japan. E-mail: park.enoch@shizuoka.ac.jp

ABSTRACT

Novel probes that can accurately (with sensitivity and specificity) detect and discriminate between the various serotypes of dengue virus (DENV) are needed for point-of-care treatment. The efficacy of a fluorophore reporter at optically transducing an ultrasensitive fluorescence intensity signal for a target nucleic acid within a molecular beacon (MB) biosensor system depends primarily on its optical properties. A new class of bright luminescent and size-dependent glutathione (GSH)-functionalized CdSe/ZnSeS core/alloyed shell quantum dots (Qdots) have been synthesized and characterized. Shell alloying tuned the photoluminescence (PL) quantum yield within the range of 23–99%, representing an approximately 2–8-fold increase over that of the binary CdSe core. In the first step of the biosensor design, gold nanoparticles (AuNPs) were conjugated to the Qdots to form AuNP-Qdot nanohybrids. In the second step, the AuNP-Qdot nanohybrids were conjugated to the 5' end of the MB. Despite the strong binding of the entities, both the AuNP-Qdot and AuNP-Qdot-MB conjugates maintained high colloidal stability. Nucleic acids of DENV1–4 were detected by the AuNP-Qdot-MB biosensors with high sensitivity, with the detection limits of the serotypes ranging from 31–260 copies/mL. The biosensor specifically discriminated between each serotype of the virus. A sensitivity comparison of a Qdot-MB with a AuNP-Qdot-MB showed that the localized surface plasmon resonance-induced signal from the AuNPs to the fluorescence intensity of the Qdots enhanced the performance of the biosensor. We have developed a new AuNP-Qdot-MB biosensor for DENV possessing high sensitivity and specificity. The new ultrasensitive assay holds great promise for the specific diagnosis of DENV, while the versatile biosensor concept is applicable to any type of RNA virus.

Keywords: Core alloyed/shell quantum dots, Gold nanoparticle, Localized surface plasmon resonance, Molecular beacon, Dengue virus

1. Introduction

The devastating health effects of dengue virus (DENV) are a global concern. The prevalence of the disease has skyrocketed within the past century, with a record of approximately 100 million cases of febrile acute disease per year.[1] DENV has four serotypes—DENV1, DENV2, DENV3 and DENV4. All of the serotypes share certain identical nucleotide sequences, which makes target-specific serotyping extremely challenging. Conventional methods such as immunochromatography, capture IgM, real-time polymerase chain reaction and IgG ELISA are limited by slow response times, low sensitivity, and high incidences of false negative results owing to serotype variation.[2–7] Novel assays that can offer ultrasensitive detection of DENV with distinct serotype-specific identification are urgently needed.

Surface plasmon resonance (SPR) has emerged as a robust sensing platform for a wide variety of analytes.[8,9] SPR can be harnessed directly in a prototype sensing device or can be used as a localized signal transducer within a sensor or biosensor platform. For the latter application, the localized SPR (LSPR) signal can be generated from plasmonic nanoparticles (NPs), which are characterized by their SPR absorption feature and can be exploited as either a sole signal transducer or as a mediator of other optical signals. SPR-based biosensors for DENV have been reported by a number of groups. Kumbhat et al. reported the serological diagnosis of DENV using an SPR-based immunosensor[10] in which the antigen of the virus was conjugated to bovine serum albumin and immobilized on a Au-coated sensor surface. Dengue antibody was thereafter used to detect the antigen, and the resulting interaction was monitored via the SPR device. Similar SPR-based technology for DENV detection have been reported by Jahanshahi et al.[11,12] and Hu et al.[13] Our proposed technique is the first to utilize the LSPR signal from plasmonic gold NPs (AuNPs) to mediate the fluorescence signal of quantum dot (Qdot) nanocrystals within a molecular beacon (MB) probe.

Single-stranded oligonucleotide probes in the form of a hairpin stem-loop structure, such as MBs, are efficient at detecting the oligonucleotide sequence of a target nucleic acid analyte.[14,15] One of the criteria when designing an ultrasensitive MB biosensor is the appropriate selection of the fluorophore reporter. Most of the fluorophore reporters used in MB assays are fluorescent organic dyes,[16] which suffer from photobleaching, poor photoluminescent (PL) stability, blinking and broad emission spectra,[17] hence limiting the sensitivity of MB-based assays. An alternative is the use of fluorescent semiconductor Qdot nanocrystals.

Colloidal fluorescent Qdot nanocrystals have attracted enormous research attention over the past two decades for a wide array of applications.[18–20] Among chemical and biological applications, highly luminescent, photostable and low-toxicity Qdots are needed for applications in biosensor design.[21,22] The advantages of fluorescent Qdots over organic fluorescent dyes are their excellent brightness, high resistance to photodegradation, narrow PL emission, and broad absorption wavelengths as well as their ability to have their emission colors tuned based on the quantum size effect.

In our attempt to develop an ultrasensitive and target-specific biosensor for DENV, we first offer an alternative method to engineer the band gap of water-soluble CdSe-based core/shell Qdots by epitaxial passivation with a ternary alloyed shell layer. Alloyed Qdots composed of more than two semiconductor chalcogenide metals have attracted significant interest because of their superior output efficiency over conventional Qdot systems and because their surface chemistry can be fabricated via band gap engineering.[23–25] Tuning the optical properties of alloyed Qdots via band gap engineering to generate spectacular optical properties is a unique way to obtain enhanced sensitivity in biosensor design. We report, for the first time, the synthesis and band gap engineering of CdSe/ZnSeS core/alloyed shell Qdots, which involved tuning their optical properties across the visible region. Ligand exchange with L-glutathione

(GSH) was used to generate hydrophilic and biocompatible Qdot nanocrystals. A cell viability assay was used to probe the cytotoxicity of the Qdots. The size-dependent GSH-CdSe/ZnSeS Qdots were used as an ultrasensitive fluorophore transducer in a MB biosensor system for DENV detection and serotyping. To boost the sensitivity of the biosensor assay, we conjugated spherical AuNPs to the Qdots to form AuNP-Qdot fluorophore conjugates. MB biosensors developed to date have utilized a non-conjugated fluorescent molecule as a fluorophore reporter, [26,27] whereas in this work, we report for the first time the utilization of a AuNP-Qdot fluorophore conjugate as the fluorophore reporter in a MB assay. The LSPR from the AuNPs was used to enhance the PL signal and boost the detection sensitivity of the biosensor. An ultrasensitive LSPR-Qdot fluorophore reporter-induced MB hybridization assay for DENV 1–4 serotypes is reported in this work, and the test results show high specificity.

2. Materials and methods

2.1. Materials

Cadmium oxide (CdO), octadecene (ODE), $HAuCl_4.3H_2O$, tannic acid, trioctylphosphine (TOP), selenium (Se), trioctylphosphine oxide (TOPO), sulfur (S), L-glutathione (GSH), oleylamine, zinc oxide (ZnO) and rhodamine 6G were purchased from Sigma Aldrich Co., LLC. (Saint Louis, MO, USA). Methanol, tri-sodium citrate, potassium hydroxide (KOH), chloroform and acetone were purchased from Wako Pure Chemical Ind. Ltd. (Osaka, Japan). Oleic acid (OA) was purchased from Nacalai Tesque, Inc. (Kyoto, Japan). An ultra-pure Milli-Q Water System (>18 MΩ·cm) was used to provide the measurement medium. The target strains DENV1–4 were purchased from Vircell Microbiologists (Granada, Spain). The MBs with DNA oligonucleotide base pairs were synthesized and purified by HPLC and purchased from FASMAC (Kanagawa, Japan). The MB was designed with 35 base pairs of single-stranded DNA labeled at the 5’ terminus with an amino group (NH_2) and at the 3’ terminus

with the black hole quencher 2 (BHQ-2) fluorescence quencher. The MB probe consisted of 25 base pairs that were complementary to DENV1–4. The resulting oligonucleotide sequences of the MBs for the detection of each DENV serotype are as follows:

DENV1: 5'-/NH_2-/**GCGAC**TGATATGTCTCTGAGTATGTATCCA**GTCGC**-BHQ2/-3'

DENV2: 5'-/NH_2-/**GCGAC**GCTCACATCTCTTAAAATGTAGCCT**GTCGC**-BHQ2/-3'

DENV3: 5'-/NH_2-/**GCGAC**GGAAATGTCCCTTAATATGTAGCCT**GTCGC**-BHQ2/-3'

DENV4: 5'-/NH_2-/**GCGAC**GTCTATCTCCTCCAGGATATATCCC**GTCGC**-BHQ2/-3'

The bold base pair sequences are the stem of the MB probe.

2.2. Characterization

UV/vis absorption and fluorescence emission measurements were performed using a filter-based multimode microplate reader (Infinite® F500, TECAN, Ltd, Männedorf, Switzerland). Transmission electron microscopy (TEM) images were obtained using a TEM JEM-2100F (JEOL, Ltd., Tokyo, Japan) operated at 100 kV. Powder X-ray diffraction (PXRD) measurements were performed using a RINT ULTIMA XRD (Rigaku Co., Tokyo, Japan) with a Ni filter and a Cu-Kα source. Data were collected from 2 theta=5–60° at a scan rate of 0.01°/step and 10 s/point. Zeta potential (ZP) and dynamic light scattering (DLS) analyses were conducted using a Zetasizer Nano series (Malvern Inst. Ltd., Malvern, UK). Energy dispersive X-ray (EDX) spectroscopy analysis was performed using a JEM-16036 LA integrated scanning electron microscope with a JED-2300 EDX. Fluorescence lifetime measurements were obtained by fluorescence lifetime imaging microscopy (FLIM) integrated with a time-resolved CMOS image sensor.[28] The instrument components included an excitation source with a 472 nm laser diode, a peak power of 48 mW and a pulse width of 120 ps. The width of the time window was 26 ns, the cycle period of the trigger signal was 192 ns, the sensor's intrinsic response to the 472-nm laser was 220 ps, and the delay step for scanning was 500 ps.

PL quantum yield (QY) measurements were performed for all the Qdots. Rhodamine 6G in ethanol was used as a reference standard ($\Phi_{Fl}^{R6G} = 0.95$).[29] The equation used to determine the PL QYs of the Qdots was as follows:

$$\Phi_{Fl}^{Qdot} = \Phi_{Fl}^{R6G} \frac{F_l^{Qdot} \cdot OD_{R6G(\lambda exc)} \cdot n^2{}_{water}}{F_l^{R6G} \cdot QD_{Qdot_{(\lambda exc)}} \cdot n^2_{ethanol}}$$

Here, Φ_{Fl}^{Qdot} is the PL QY of the Qdots, Φ_{Fl}^{R6G} is the PL of the standard, $F_l^{QD}$and F_l^{R6G} are the integrated sums of the PL intensity of the Qdots and standard, $OD_{R6G(\lambda exc)}$ and $OD_{Qdot_{(\lambda exc)}}$ are the optical densities of the standard and Qdots at the excitation wavelength, and $n^2{}_{water}$ and $n^2_{ethanol}$ are the refractive indexes of water and ethanol, respectively.

2.3. Preparation of the precursors

The TOPSe precursor was used to introduce the Se metal anion in the formation of the CdSe binary core and the ternary alloyed ZnSeS shell. Briefly, 1.93 g of TOPO was dissolved in 25 mL of ODE and heated until the TOPO surfactant was completely dissolved. Then, 0.3 g of Se was added, and the mixture was sonicated for several minutes and stirred at room temperature.

The TOPS precursor was prepared to introduce the S metal during the formation of the ternary alloyed ZnSeS shell layer. First, 1.93 g of TOPO was dissolved in 30 mL of ODE and 20 mL of OA. The solution was heated to ensure the complete dissolution of the TOPO surfactant. Then, 0.16 g of S was added to the mixture, and the mixture was sonicated for several minutes. Afterward, the solution was heated to aid the dissolution of the S metal and sonicated again to ensure the complete dissolution of the S metal. Finally, the solution was stirred at room temperature.

ZnO was used as the sole precursor to introduce Zn during the formation of the ternary alloyed ZnSeS shell layer. To a solution of 30 mL of ODE and 20 mL of OA, 0.4 g of ZnO was added. The mixture was sonicated for several minutes and stirred under ambient conditions.

2.4. Hot-injection organometallic synthesis of CdSe/ZnSeS Qdots (Scheme 1)

The synthesis of CdSe/ZnSeS core/alloyed shell Qdots was similar to a method used for the fabrication of alloyed core/shell Qdots but with some modifications.[30] In a 3-necked round-bottom flask fitted with a thermometer, an Ar gas inlet and a refluxing condenser, 1.3 g of CdO, 1.93 g of TOPO, 2 mL of TOP, 5 mL of oleylamine, 50 mL of ODE and 30 mL of OA were stirred and heated. The formation of the Cd-TOPO-TOP-OA-oleylamine complex was evident from the steady change in color of the precursor solution at elevated temperature. The TOPSe precursor was added to the Cd-TOPO-TOP-OA-oleylamine solution at a temperature >220°C to initiate the nucleation and growth of the CdSe core. Once an appropriate growth of CdSe Qdots was achieved, epitaxial overgrowth of the ternary shell layer was achieved by adding appropriate amounts of the ZnO, TOPSe and TOPS precursor solutions. The temperature of the solution (240–300°C) was used to control the size of the Qdots. CdSe/ZnSeS core/alloyed shell Qdots of different sizes were removed from the solution at different time intervals. The Qdots were washed in methanol and acetone and subsequently stored in chloroform. Six different sizes of GSH-CdSe/ZnSeS core/alloyed shell Qdots were produced in this work; these were denoted by Qdot582, Qdot594, Qdot606, Qdot614, Qdot618 and Qdot622 according to their PL emission wavelengths.

2.5. Ligand exchange reaction with GSH and purification

The ligand exchange of the hydrophobic capping of the Qdots with the GSH thiol ligand was performed in a methanolic-KOH-GSH-water solution. First, 3 g of KOH was dissolved in 40 mL of methanol, and 2 g of GSH was added and dissolved via ultrasonication. Then, chloroform-dispersed Qdots of different sizes were added separately into different portions of the methanolic-KOH-GSH solution, and an appropriate amount of Millipore water was added.

The Qdot solution was stirred for several minutes and allowed to stand until the next day. Effective purification of the Qdots is essential to preserve their fluorescence, hence a seven-step procedure was used to purify the nanocrystals to ensure that they were free from embedded organic capping. The steps were as follows: step 1 → acetone, step 2 → chloroform, step 3 → acetone/chloroform, step 4 → water/acetone/chloroform, step 5 → acetone/chloroform, step 6 → chloroform and step 7 → acetone.

2.6. Synthesis of L-cysteine-capped AuNPs

First, citrate-capped AuNPs were synthesized according to literature procedures.[31] Then, a ligand exchange reaction using a methanolic-KOH-L-cysteine solution was used to stabilize the AuNPs with L-cysteine. Briefly, 3 g of KOH was dissolved in 40 mL of methanol via ultrasonication, and 2 g of L-cysteine was added into the solution and sonicated. The prepared KOH-methanol-L-cysteine solution was then added into the citrate-capped AuNP solution and stirred for several minutes for the ligand exchange reaction to occur. The L-cysteine-capped AuNPs were purified by centrifugation at 1500 g for 10 min.

2.7. Conjugation of the Qdots to the AuNPs and MBs

To develop the biosensor probe for DENV1–4, optimum concentrations of Qdot582, Qdot594, Qdot606 and Qdot618 were used for conjugation. Briefly, 1 mL of 0.1 M EDC solution was added to 1 mL of aqueous L-cysteine AuNPs (11.5 nM) to activate the carboxylate groups. The solution was stirred at ambient temperature for ~30 min. Next, 4 mL of 0.45 mg/mL Qdot582, Qdot594, and Qdot606 and 0.30 mg/mL Qdot618 were each added to separate solutions of the EDC-activated L-cysteine AuNPs. To stabilize the amide bond, 1 mL of 0.1 M NHS was added. The reaction was allowed to proceed for ~30 min. The Qdot-AuNP conjugates were purified

and concentrated by centrifugation (1,500 g for 3 min) using a 30,000 micron molecular weight cut-off Nanosep® centrifugal filter (Pall Co., Port Washington, NY, USA).

The Qdot-AuNP-MB conjugate biosensor was produced by adding 500 µL of 0.1 M EDC into 3.5 mL of aqueous Qdot-AuNP conjugates to activate the free carboxylate groups present in the conjugated Qdots. The reaction was stirred for ~30 min, after which 500 µL of 0.5 M MB solution (in Tris-EDTA buffer) and 500 µL of 0.1 M NHS were added; the reaction was then stirred for ~30 min under ambient conditions. The Qdot-AuNP-MB conjugates were purified using the same purification procedure used for the Qdot-AuNP conjugates. The biosensor conjugates were stored at 4°C prior to use.

2.8. Procedures for the Qdot-LSPR-induced MB-hybridized detection of DENV

DENV1–4 were detected using the Qdot-LSPR-induced MB bioprobe. In a 96-well plate, 10 µL of the Qdot-AuNP-MB conjugate solution was mixed with 40 µL of buffer solution and 5 µL of the DENV target. This system was used for the detection of DENV1, DENV2 and DENV3. For the detection of DENV4, 2 µL of the probe solution was mixed with 48 µL of buffer solution and 5 µL of the DENV4 target. The probe solution was allowed to hybridize with the DENV target for 3 min, after which the fluorescence emission was measured. The probe solution was excited at 470 nm, and the PL emission range was from 480–800 nm.

3. Results and discussion

3.1. Fabrication of the GSH-CdSe/ZnSeS Qdots

We used a one-step synthesis procedure to fabricate the CdSe/ZnSeS core/alloyed shell Qdots. Scheme 1 shows the synthesis steps used in the fabrication of the Qdots. The Cd precursor was prepared in ODE, a non-coordinating solvent, and it was chemically coordinated to TOPO, TOP, oleylamine and OA, which acted as stabilizers (Step 1). The initial color of the Cd-

TOPO-TOP-OA-oleylamine solution was deep brown, but at elevated temperature, the color of the reaction solution gradually shifted to pale yellow. The color change corresponds to the complexation of Cd to the organic capping ligands.

An important criterion in controlling the size and quality of the core/alloyed shell Qdots is the temperature at which the CdSe core is passivated. Passivation of the CdSe seeds at a higher temperature (≥260°C) allows the dots to grow via Ostwald ripening, which leads to a polydisperse size distribution, a broad PL emission line and a deep trap emission. Conversely, reduced crystallinity of the shell material or incomplete decomposition of the precursors are factors that affect the quality of the core/alloyed shell Qdots if the CdSe core is coated at a relatively low temperature (<200°C)**.**[32] To produce highly crystalline core/alloyed shell Qdots and to ensure a constant size distribution of the core, the growth temperature was determined independently for each core/alloyed shell size. In addition, the concentrations of the shell precursors, their molar ratios, and the rates of injection into the CdSe growth solution were crucial in determining the quality of the core/alloyed shell Qdots.

Our primary objective is to produce highly luminescent, water-soluble core/alloyed shell Qdot nanocrystals that can be used as ultrasensitive fluorophore reporters in our proposed biosensor system. To achieve this goal, we transferred the organic phase Qdots to the water-soluble phase using a ligand exchange reaction with GSH as a thiol-capping agent (Step 2). After the ligand exchange reaction, a seven-step purification strategy was developed for the total removal of the unreacted organic capping from the Qdot surfaces. The purification strategy was effective in producing high-quality Qdots and preserving their fluorescence. Six different sizes of GSH-CdSe/ZnSeS core/alloyed shell Qdots were produced in this work; these were denoted by Qdot582, Qdot594, Qdot606, Qdot614, Qdot618 and Qdot622, according to their PL emission wavelengths.

3.2. Morphology of the GSH-CdSe/ZnSeS Qdots

TEM was used to probe the morphology of the Qdot nanocrystals and to determine their size and shape distributions. Figs. 1A–F show the TEM images of the size-dependent GSH-CdSe/ZnSeS Qdots. The particles in each image display a homogenous size distribution, which can be attributed to the manner in which the dots nucleate and grow. Tentatively, we can infer that homogenous nucleation of the core/alloyed shell Qdots prevails at the core/shell interface, leading to epitaxial particle growth and a quasi-spherical shape morphology. The estimated average sizes of the Qdots are 1.9±0.4 nm for Qdot582, 3.9±1.0 nm for Qdot594, 4.2±0.6 nm for Qdot606, 4.3±0.7 nm for Qdot614, 4.4±0.9 nm for Qdot618 and 4.6±0.7 nm for Qdot622. Interfacial alloying between the ZnSeS shell and the CdSe core is believed to increase the particle uniformity of the Qdots. The corresponding particle size distribution histograms are shown in Figs. A1-F1.

3.3. DLS and ZP

The modulation of the scattered light intensity from the laser that penetrates the Qdot colloidal solution was analyzed by DLS as a function of time to determine the hydrodynamic particle size distribution. Generally, larger colloidal particles diffuse more slowly than smaller particles, and DLS provides a correlation function that mathematically corresponds to the particle size based on the time dependence of the light being scattered. This phenomenon can also be used to probe for particle aggregation by comparing the hydrodynamic size with the particle size obtained from TEM. For a non-aggregated Qdot colloidal solution, the measured hydrodynamic size will be slightly larger than or similar to the TEM size. However, for an aggregated Qdot colloidal solution, a high polydispersity index resulting from the large variability in size causes the hydrodynamic size to be far larger than the TEM size, typically >100 nm. Figs. 2A–F show the DLS curves for the different sizes of GSH-CdSe/ZnSeS

core/alloyed shell Qdots. Each DLS curve shows a relatively narrow hydrodynamic size distribution. The measured hydrodynamic sizes are 4.1±1.0 nm for Qdot582, 6.8±2.0 nm for Qdot594, 7.4±1.7 nm for Qdot606, 7.9±2.1 for Qdot614, 8.4±2.4 for Qdot618 and 8.7±2.6 for Qdot622. Given the closeness of the hydrodynamic sizes to the TEM sizes, it is reasonable to conclude that the size-dependent GSH-CdSe/ZnSeS Qdots are monodisperse and non-agglomerated.

The potential at the shear/slipping plane of a colloidal nanoparticle moving under the influence of an applied electric field is known as the electrokinetic potential or ZP.[33] The electric potential reflects the amount of work required to transport (without acceleration) a unit positive charge with affinity to the surface of the nanoparticle. When a colloidal particle is dispersed in solution, an electric double layer (EDL), also known as an adsorbed double layer, is created on the surface. The inner layer of the EDL consists primarily of molecules/ions with charges opposite to the colloidal particles (i.e., the Stern layer). Therefore, the fundamental principle of the ZP relates to the potential difference between the EDL of an electrophoretic mobile particle and the surrounding layer of dispersant at the slipping plane.[34]

The chemical, biological and physical effects of nanoparticles in living systems are dependent on their physicochemical properties. The surface charge of a nanoparticle is one of the factors that determines its biological properties, such as colloidal stability and cellular uptake.[34] One of the most important applications of the ZP is as a measure of the colloidal stability of nanoparticles. A common guideline for the ZP in drug delivery is as follows: ±30 mV=highly stable, ±20–30 mV=moderately stable, ±10–20 mV=relatively stable and ±0–10 mV=highly unstable.[35] Figs. 2A1–F1 show the ZP curves for the size-dependent GSH-CdSe/ZnSeS core/alloyed shell Qdots. The number of GSH thiol ligands on the surfaces of the Qdots is not expected to be the same; thus, the steric repulsion of the GSH ligands is expected to influence the overall ZP values. The following ZP values are obtained: -56.6±4.9 mV for

Qdot582, -52.9±4.9 mV for Qdot594, -36.0±8.9 mV for Qdot606, -54.4±7.9 mV for Qdot614, -55.1±4.9 mV for Qdot618 and -57.6±9.5 mV for Qdot622. The values obtained are within the range of high colloidal stability, indicating that the Qdots are highly stable and have the potential to be used as fluorophore reporters in biosensor design.

3.4. Crystal structure of the Qdots

PXRD was used to probe the crystal structure of the core/alloyed shell Qdots and the lattice parameters of the ZnSeS shell and CdSe core. Fig. 3A shows the diffraction patterns of the GSH-CdSe core and the GSH-CdSe/ZnSeS Qdots. The crystalline diffraction pattern exhibited by GSH-CdSe is weaker than that of the size-dependent GSH-CdSe/ZnSeS Qdots. The three prominent diffraction peaks for the GSH-CdSe/ZnSeS Qdots correspond to the dominant zinc-blend crystal structure, with diffraction planes at {111}, {220} and {311}. The diffraction patterns for the GSH-CdSe/ZnSeS Qdots are indicative of a strong passivating effect of the alloyed ZnSeS shell on the bare CdSe core. Also notable in the diffraction pattern is the shift in the diffraction peak of the core/alloyed shell Qdots to a higher Bragg angle than that of the core. The shift is clearly noticeable in the first {111} plane for Qdot606–Qdot622. The shift is a reflection of ZnSeS shell alloying on the bare CdSe.

The lattice parameter of ZnSeS was simulated from the XRD pattern to determine the lattice mismatch between the core and alloyed shell. The average lattice constant of ZnSeS simulated from the XRD spectra of the different-sized core/alloyed shell Qdots was 5.928 Å. Thus, we calculated the lattice mismatch between CdSe (lattice constant 6.050 Å) and ZnSeS to be 2%. This low lattice mismatch suggests that the core/alloyed shell Qdots are less susceptible to interfacial strain and dislocation. It is therefore reasonable to assume that the optical properties of GSH-CdSe/ZnSeS Qdots can be precisely tuned with variable PL QY across the regime of quantum confinement.

3.5. EDX

EDX was used to qualitatively and quantitatively probe the cation and anion metal chalcogenide elements present in the core and core/alloyed shell Qdots. We selected the binary GSH-CdSe core and the Qdot606 core/alloyed shell as representative Qdots for this analysis. Figs. 3B and C show the EDX spectra for the GSH-CdSe and Qdot606 Qdots. Elemental peaks for Cd, Se, S, C and O were confirmed for the GSH-CdSe Qdots. The presence of S, C and O indicates the presence of functional groups in the surface-capped GSH ligand. For Qdot606, elemental peaks for Cd, Se, Zn, S, C and O were confirmed. A new peak associated with Zn is seen at ~1.00 keV. The elemental composition for GSH-CdSe is as follows: Cd (57.12%), Se (3.5%), S (13.74), O (9.21%), and C (16.43). The values for Qdot606 are as follows: Cd (51.19%), Se (8.59%), Zn (2.05%), S (11.67%), O (8.07%) and C (18.43%).

3.6. Size-dependent optical properties and their influence on the PL QY

The size-dependent optical properties of the GSH-CdSe/ZnSeS Qdots were studied. Figs. 4A and B show the evolution of the PL emission and absorption spectra of the size-dependent Qdots. The PL emissions of the Qdots were tuned from 580 nm to 622 nm as the absorption spectra were tuned from 574 nm to 612 nm. The Qdots exhibited a narrow emission line with a full width at half maximum in the range of 34–40 nm. The band gap of the Qdots was tuned from 2.14 to 2.00 eV. The size increase of the Qdots reflects the red-shifting of the PL emission spectra and corresponds to a decreasing band gap. The band gap variation implies that the core/alloyed shell Qdots grew within the regime of quantum confinement.

Fig. 4A shows the variation in the PL QY as a function of the PL emission wavelength. The variation in the photophysical properties of the QDs indicates that the PL QY is independent of the Qdot size. The tuning of the PL QY from 23% to 99% is a direct confirmation of the effective passivation of the ZnSeS alloy on the CdSe core, representing a

~2–8-fold increase in PL QY. Factors that influence the Qdot surface passivation are the reaction time, temperature, precursor concentration, precursor materials and amount of precursor. The combination of these factors and their use in the synthesis process determine the overall quality of the Qdots. The PL QY is unique to each Qdot size. The near-perfect PL QY of 99% for Qdot606 indicates the complete suppression of the non-radiative exciton recombination state.

Cell viability assays of Qdot606 on HEK 293T cells showed that the Qdots posed no toxicity to the cells at mg/mL doses. A detailed discussion of the cell viability assay and PL lifetime measurements of the Qdots are presented in Supplementary Figs. S-1 and S-2.

3.7. Biosensor application

3.7.1. Detection mechanism of the biosensor

Scheme 2 shows the descriptive detection mechanism of the biosensor. L-cysteine AuNPs are conjugated to GSH-CdSe/ZnSeS Qdots (Qdot582, Qdot594, Qdot606 and Qdot618) to form their respective Qdot-AuNP conjugates (Step 1 in Scheme 2). The free carboxylate groups on the bonded Qdot-AuNP surface are then activated and conjugated to the amino moiety of the MB. The loop sequence of the MB is designed with complementary DNA oligonucleotide base pairs to the single RNA strand of DENV. The conjugation of the Qdot-AuNP conjugates to the MB biosensor causes the Qdot-AuNP LSPR fluorophore and the black hole quencher-2 (BHQ-2) fluorescence quencher to be in close proximity. This close proximity triggers non-radiative exciton recombination states in the Qdot-AuNP, thereby quenching its fluorescence (Step 2 in Scheme 2). In the presence of the target DENV, the distance between the MB and the Qdot-AuNP fluorophore reporter is stretched. Thus, the occurrence of the DNA/RNA heteroduplex hybridization triggers an LSPR-induced fluorescence increase that is proportional to the concentration of the target virus.

3.7.2. Characterization of the L-cysteine-capped AuNPs

UV/vis, TEM, DLS and ZP were used as complementary techniques to characterize the L-cysteine-capped AuNPs. Fig. 4C shows the UV/vis absorption spectrum of the L-cysteine AuNPs, exhibiting a typical SPR peak at an absorption maximum of 538 nm. The TEM image in Fig. 4D displays the spherical morphology of the AuNPs, with an average size of 7.3±2.7 nm as determined from the particle size distribution histogram (Fig. 4E). Fig. 4F shows the DLS plot with a hydrodynamic particle size of 16.07±4.3 nm. The hydrodynamic particle size value validates the monodisperse nature of the AuNPs and represents an unagglomerated colloidal state. The colloidal stability of the AuNPs was investigated using ZP as shown in Fig. 4F. A ZP value of -48.5±5.6 mV was obtained. The ZP value is an indication that our synthesized L-cysteine-capped AuNPs exhibit high colloidal stability.

3.7.3. Characterization of the Qdot-AuNP and Qdot-AuNP-MB nanoconjugates

The binding effects of the Qdots to the AuNPs (1:1, v/v) and MBs are discussed in this section. Figs. 5A–D show the TEM images of the Qdot582-AuNP, Qdot594-AuNP, Qdot606-AuNP and Qdot618-AuNP conjugates, respectively. From the morphology of the conjugates, it is clear that the Qdots and AuNPs are well dispersed in each image. The gray particles and the dark particles in each image show the Qdots and the AuNPs, respectively. Several of the AuNPs are well embedded within the Qdot ensemble. The particle distribution confirms the strong binding effects of the Qdots to the AuNPs. The corresponding TEM images of the Qdot582-AuNP-MB, Qdot594-AuNP-MB, Qdot606-AuNP-MB and Qdot618-AuNP-MB conjugates are shown in Supplementary Figs. S-3A–D, respectively. The particle morphology reveals the strong binding of the Qdot-AuNP conjugates to the MBs, as evidenced by the coarseness of the particles. Discussion of the DLS, ZP and fluorescence quenching effects of the Qdot-AuNP and Qdot-AuNP-MB conjugates is provided in Supplementary Figs. S-4, S-5 and S-6.

3.7.4. LSPR-induced hybridization for the detection of DENV

Detecting extremely low-copy-number RNA viruses without a pre-amplification step requires a biosensor that can transduce an ultrasensitive signal. In this work, we challenged our biosensor with the detection of extremely low copy numbers of DENV1–4 to evaluate its ultrasensitivity. Qdot582-AuNP-MB was used for DENV1 detection, Qdot594-AuNP-MB for DENV2, Qdot606-AuNP-MB for DENV3 and Qdot618-AuNP-MB for DENV4. Figs. 6A–D show the fluorescence signal emission spectra for the detection of DENV1–4. The progressive PL enhancement of the biosensor probe is directly proportional to the concentration of DENV. DENV1 was detected from 20–120 copies/mL, DENV2 from 20–100 copies/mL, DENV3 from 20–80 copies/mL and DENV4 from 20–80 copies/mL. The corresponding fluorescence signal calibration curves are shown in Figs. 6E–H. We can directly draw the conclusion that our LSPR-induced hybridized biosensor was highly sensitive and could detect extremely low concentrations of DENV. The limit of detection (LOD) was determined by multiplying the standard deviation of blank measurements (n=10) by 3 and then dividing by the slope of the calibration curve. The LOD obtained was 260 copies/mL for DENV1, 31 copies/mL for DENV2, 75 copies/mL for DENV3 and 65 copies/mL for DENV4. A comparison of the detection sensitivities of the Qdot-AuNP-MB biosensor probe and the Qdot-MB probe (with no influence from LSPR signals from AuNPs) is provided in Supplementary Fig. S-7. The data show that the magnitude of fluorescence enhancement was higher for the Qdot-AuNP-MB biosensor probe than for the Qdot-MB probe (with no influence from LSPR signals from AuNPs).

3.7.5. Serotyping of DENV

Developing a biosensor that is capable of the specific serotyping of DENV1–4 is extremely challenging because each DENV serotype has a number of similar base pair sequences, making

the DENV serotypes difficult to distinguish. This similarity implies that complementary hybridization can occur because of interference between a DENV serotype and the target DENV RNA. Our characterization of specific serotyping is quantified by the degree of fluorescence enhancement for the target DENV serotype compared to that of the negative control. Here, the negative controls are the DENV serotypes that do not have full sequence complementarity to the target probe. The serotyping of the DENV strains was performed at the highest concentration detected by our designed biosensor probe.

Figs. 7A–D show the data for the specific serotyping of the DENV targets. For the serotyping of DENV1 at 120 copies/mL (Fig. 7A), the negative controls (DENV2, DENV3 and DENV4) at the same concentration did not enhance the fluorescence of the biosensor probe, thus confirming the specificity of Qdot582-AuNP-MB for DENV1. For the serotyping of DENV2 at 100 copies/mL (Fig. 7B), the negative controls (DENV1, DENV3 and DENV4) enhanced the fluorescence of the probe, but the degree of enhancement was much lower than for the target DENV2. The enhancement occurred because DENV1, DENV3 and DENV4 have 14, 18 and 11 complementary base pairs, respectively, to the target Qdot594-AuNP-MB probe for DENV2. Similar fluorescence enhancement from the negative controls (DENV1, DENV2 and DENV4) is also observed in Fig. 7C for the serotyping of DENV3 (80 copies/mL). Our analysis showed that the DENV1, DENV2, and DENV4 negative controls have 18, 18 and 13 complementary base pairs, respectively, to the target Qdot606-AuNP-MB probe for DENV3. However, judging from the differences in fluorescence enhancement for DENV2 and DENV3 against the negative controls, we can tentatively conclude that the biosensor probe is specific for the target DENV and can distinguish between different serotypes of the virus. The serotyping of DENV4 (80 copies/mL) induced a noticeable fluorescence enhancement (Fig. 7D) compared to that of the negative controls (DENV1, DENV2 and DENV3). This finding

confirms that the biosensor probe is indeed specific to the target DENV and is suitable for distinguishing between DENV serotypes.

4. Conclusions

An ultrasensitive and serotype-specific biosensor for DENV serotypes has been developed. To construct the MB, we synthesized and characterized new GSH-capped core/alloyed shell Qdots. L-cysteine-capped AuNPs were conjugated to four different sizes of the Qdots to form AuNP-Qdot hybrids. Subsequently, the AuNP-Qdot hybrids were conjugated to the MB to form AuNP-Qdot-MB biosensor probes with the AuNP-Qdots utilized as the fluorophore reporter. The biosensor operates by hybridizing the DNA loop sequence of the MB with the single RNA strand of DENV, thereby triggering an LSPR signal from the bound AuNPs to the Qdots and thus producing a fluorescence signal in proportion to the concentration of the target DENV. LSPR from the AuNPs bound to the Qdots was used as a signal booster. Ultrasensitive detection of DENV down to 20 copies/mL was achieved. We have overcome the problem associated with most conventional probes for DENV by specifically distinguishing different serotypes of the virus. We anticipate that this new class of biosensor will be applicable for the detection of low-level RNA viruses without the need for a pre-amplification step.

Acknowledgments

A Japan Society for the Promotion of Science (JSPS) postdoctoral fellowship for overseas researchers (P13454) offered by the JSPS is gratefully acknowledged. This work was supported by the Heiwa Nakajima Foundation and a Grant-in-Aid for a JSPS fellow (No. 26-04354). We thank Rina Baba for assistance with the MTT assay, Kenshin Takemura for assistance with the

EDX measurements, and Min-Woong Seo and Shoji Kawahito for assistance with the PL lifetime measurements.

References

1 H. B. Scott, *Lancet*, 2007, **370**, 1644–1652.

2 A. J. Baeumner, N. A. Schlesinger, N. S. Slutzki, J. Romano, E.M. Lee, R.A. Montagna, *Anal. Chem.*, 2002, **74**, 1442–1448.

3 S. H. Chen, Y. C. Chuang, Y. C. Lu, H. C. Lin, Y. L. Yang, C. S. Lin, *Nanotechnology*, 2009, **20**, 215501.

4 M. S. Cheng, J. S. Ho, C. H. Tan, J. P. S. Wong, L. C. Ng, C.-S. Toh, *Anal. Chim. Acta*, 2012, **725**, 74–80.

5 A. C. M. S. Dias, S. L. R. Gomes-Filho, M. M. S. Silva, R. F. Dutra, *Biosens. Bioelectron.*, 2013, **44**, 216–221.

6 S, Kumbhat, K, Sharma, R, Gehlot, A. Solanki, V, Joshi, *J. Pharm. Biomed. Anal.*, 2010, **52**, 255–259.

7 S. Kwakye, V. N. Goral, A. J. Baeumner, *Biosens. Bioelectron.*, 2006, **21**, 2217–2223.

8 A. Chhatre, P. Solasa, S. Sakle, R. Thaokar, A. Mehra, *Coll. Surf. Physicochem. Eng. Asp.*, 2012, **404**, 83–92.

9 A. Shalabney, I. Abdulhalim, *Opt. Lett.*, 2012, **37**, 1175–1177

10 S. Kumbhat, K. Sharma, R. Gehlot, A. Solanki, V. Joshi, *J. Pharm. Biomed. Anal.*, 2010, **5**, 255–259.

11 P. Jahanshahi, E. Zalnezhad, S. D. Sekaran, F. R. M. Adikan, *Sci. Reports*, 2014, **4**, 3851.

12 P. Jahanshahi, S. D. Sekaran, F. R. M. Adikan, *Med. Biol. Eng. Comput.*, 2015, **53**, 679–687.

13 D. Hu, S. R. Fry, J. X. Huang, X. Ding, L. Qiu, Y. Pan, Y. Chen, J. Jin, C. McElnea, J. Buechler, X. Che, M. A. Cooper, *Biosensors,* 2013, **3**, 297–311.

14 S. Bernacchi, Y. Mely, *Nucleic Acids Res.,* 2001, **29**:E62.

15 T. Heyduk, A. Heyduk, *Nat. Biotechnol.,* 2002, **20**, 171–175.

16 G. Goel, A. Kumar, A. K. Puniya, W. Chen, K. Singh, *J. Appl. Microbiol.,* 2005, **99**, 435–442.

17 P. J. Santangelo., *Wiley Interdiscip. Rev. Nanomed. Nanobiotechnol.,* 2010, **2**, 11–19.

18 M. P. Bruchez, M. Moronne, P. Gin, S. Weiss, A. P. Alivisatos, *Science,* 1998, **281**, 2013–2016.

19 S. Coe, W-K. Woo, M. G. Bawendi, V. Bulovic, *Nature,* 2002, **420,** 800–803.

20 S. K. Poznyak, D. V. Talapin, E. V. Shevchenko, H. Weller, *Nano Lett.,* 2004, **3**, 693–698.

21 E. Tully, S, Hearty P. Leonard, R. O'Kennedy, *Int. J. Biol. Macromol.,* 2006, **39**, 127–134.

22 L. Zhu, S. Ang, W. T. Liu, Appl. Environ. *Microbiol.,* 2004, **70**:597–598.

23 K. Boldt, N. Kirkwood, G. A. Beane, *Chem. Mater.,* 2013, **25**, 4731-4738.

24 J. Ouyang, C. I. Ratcliffe, D. Kingston, B. Wilkinson, J. Kuijper, X. Wu, J. A. Ripmeester, K. Yu, *J. Phys. Chem. C,* 2008, **112**, 4908–4919.

25 M. D. Regulacio, M.-Y. Han, *Accounts Chem. Res.,* 2010, **43**, 621–630.

26 N. C. Cady, A. D. Strickland, C. A. Batt, *Mol. Cell Probe,* 2007, **21**, 116–124.

27 J. H. Kim, D. Morikis, M. Ozkan, *Actuat B-Chem.,* 2004, **102,** 315–319.

28 M.-W. Seo, K. Kagawa, K. Yasutomi, T. Takasawa, Y. Kawata, N. Teranishi, Z. Li, I. A. Halin, S. Kawahito, *IEEE Int. Solid-State Circuits Conf. (ISSCC) Dig Tech Papers,* 2015, 198–199.

29 R. F. Kubin, A. N. Fletcher, *J. Lumin.,* 1982, **27**, 455–462.

30 O. Adegoke, M.-W. Seo, T. Kato, S. Kawahito, E. Y. Park, *J. Mater. Chem. B* 2016, **4**, 1489–1498.

31 J. W. Slot, H. J. Gueze, A. J. Weerkamp, *Method Microbiol.*, 1988, **20**, 211–236.

32 B. O. Dabbousi, J. Rodriguez-Viejo, F. V. Mikulec, J. R. Heine, H. Mattoussi, R. Ober, K. F. Jensen, M. G. Bawendi, *J. Phys. Chem. B*, 1997, **101**, 9463–9475.

33 M. Kaszuba, J. Corbett, F. M. Watson, A. Jones, *Philos. Transact. A Math Phys. Eng. Sci.*, 2010, **368**, 4439–4451.

34 V. R. Patel, Y. K. Agrawal, *J. Adv. Pharm. Technol. Res.*, 2011, **2**, 81–87.

35 S. Bhattacharjee, *J. Control Release, 2016*, **235**, 337–351.

Figure legends

Scheme 1 Schematic representation of the hot-injection synthesis of CdSe/ZnSeS core/alloyed shell Qdots and the subsequent ligand exchange reaction with GSH. Emission colors of the Qdots taken under UV light are displayed

Scheme 2 Schematic representation of the biosensor probe containing the Qdot-AuNP conjugate, binding of the Qdot-AuNP to the MB and the subsequent LSPR-induced MB hybridization (**A**) Conjugation of L-cysteine AuNPs to GSH-CdSe/ZnSeS Qdots. (**B**) Conjugation of the Qdot-AuNP conjugate to the MB and subsequent detection principle of the biosensor

Fig. 1 Morphology and size distribution histogram of GSH-CdSe/ZnSeS Qdots. TEM images of (**A, A1**) Qdot582, (**B, B1**) Qdot594, (**C, C1**) Qdot606, (**D, D1**) Qdot614, (**E, E1**) Qdot618 and (**F, F1**) Qdot622

Fig. 2 DLS and zeta potential curve. (**A, A1**) Qdot582, (**B, B1**) Qdot594, (**C, C1**) Qdot606, (**D, D1**) Qdot614, (**E, E1**) Qdot618 and (**F, F1**) Qdot622

Fig. 3 Crystal structure of the Qdots. (**A**) PXRD pattern for GSH-CdSe core and the respective GSH-CdSe/ZnSeS Qdots denoted by Qdot582, Qdot594, Qdot606, Qdot614, Qdot618 and Qdot622. EDX spectrum of (**B**) GSH-CdSe core and (**C**) Qdot606

Fig. 4 Size-dependent optical properties of the Qdots. PL emission (**A**) and UV/vis absorption (**B**) of Qdot582, Qdot594, Qdot606, Qdot614, Qdot618 and Qdot622. Characterization of L-cysteine-AuNPs. (**C**) UV/vis absorption spectrum, (**D**) TEM image, (**E**) particle size distribution histogram, (**F**) DLS plot and (**F**) ZP curve

Fig. 5 Morphology of GSH-CdSe/ZnSeS Qdots-AuNP nanoconjugates. TEM images of (**A**) Qdot582-AuNP, (**B**) Qdot594-AuNP, (**C**) Qdot606-AuNP and (**D**) Qdot618-AuNP

Fig. 6 Detection of DENV1–4 using QDs-AuNP-MB nanoconjugates. Fluorescence switch on detection for dengue virus (**A–D**) and the corresponding PL calibration curves (**E–H**). (**A, E**) Qdot582-AuNP-MB for DENV1, (**B**, **F**) Qdot594-AuNP-MB for DENV2, (**C, G**) Qdot606-AuNP-MB for DENV3 and (**D, H**) Qdot618-AuNP-MB for DENV4. The inset of **E**, **F** and **G** are the linear calibration plot

Fig. 7 Specificity of serotyping of DENV. Specificity for (**A**) DENV1, (**B**) DENV2, (**C**) DENV3 and (**D**) DENV4. The negative control is indicated in each figure

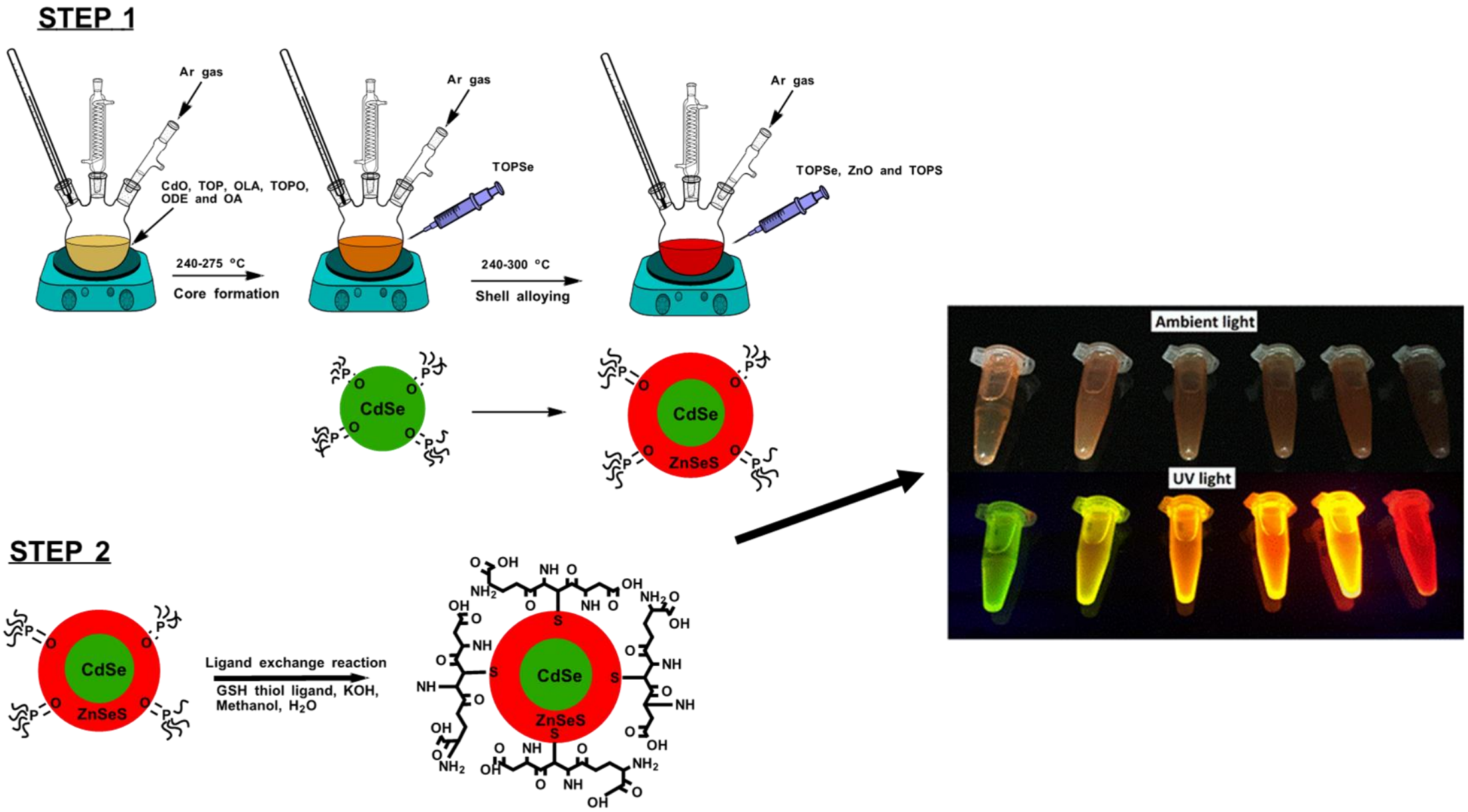
STEP 1
Ar gas
CdO, TOP, OLA, TOPO, ODE and OA
240-275 °C
Core formation
Ar gas
TOPSe
240-300 °C
Shell alloying
Ar gas
TOPSe, ZnO and TOPS
CdSe
CdSe
ZnSeS
Ambient light
UV light
STEP 2
CdSe
ZnSeS
Ligand exchange reaction
GSH thiol ligand, KOH,
Methanol, H2O
CdSe
ZnSeS

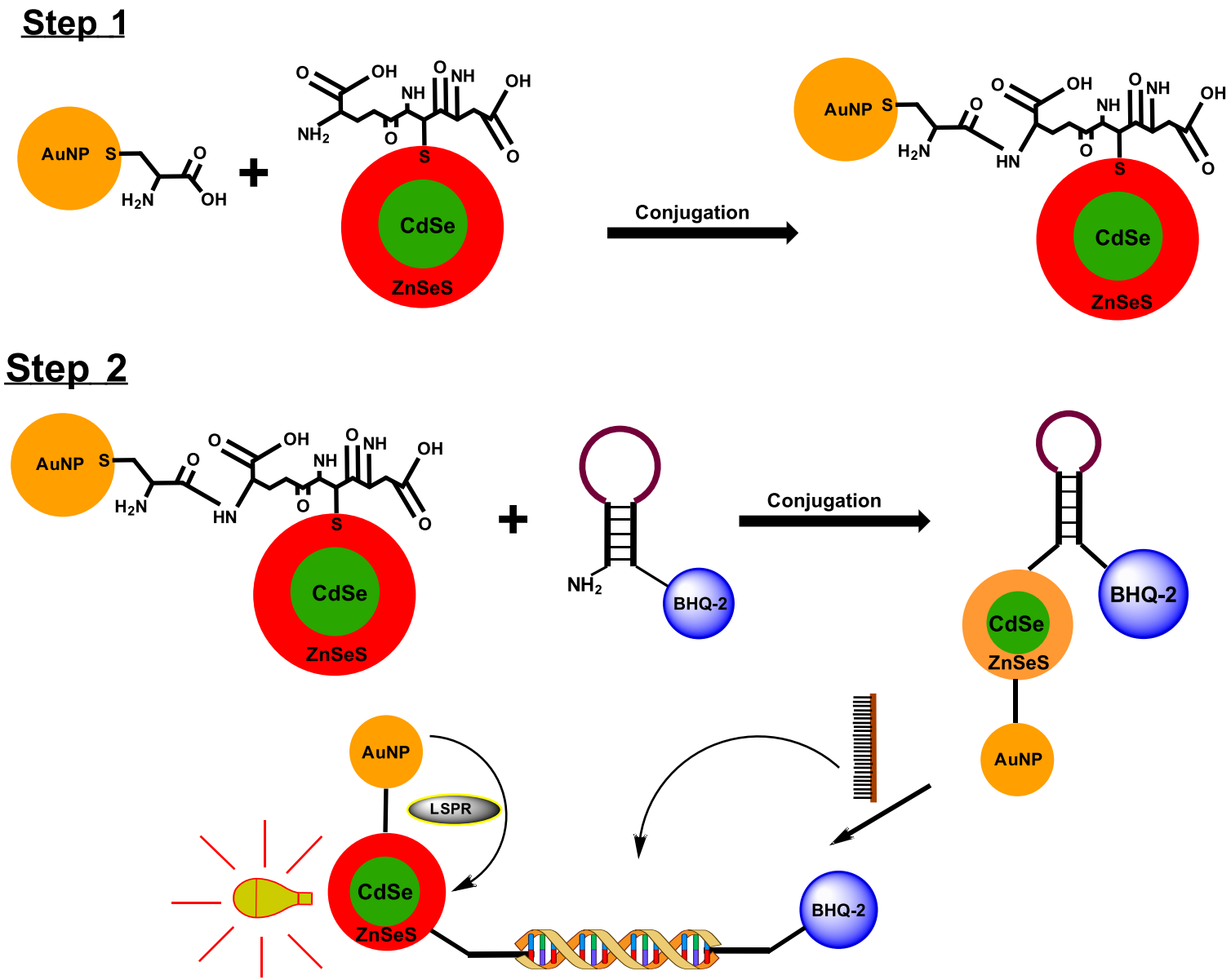
Step 1
AuNP
S
O
OH
H_2N
OH
NH
O
NH
OH
NH_2
O
S
CdSe
ZnSeS
Conjugation
AuNP
S
O
OH
NH
O
NH
OH
H_2N
HN
O
S
O
CdSe
ZnSeS
Step 2
AuNP
S
O
OH
NH
O
NH
OH
H_2N
HN
O
S
O
CdSe
ZnSeS
NH_2
BHQ-2
Conjugation
CdSe
ZnSeS
BHQ-2
AuNP
AuNP
LSPR
CdSe
ZnSeS
BHQ-2

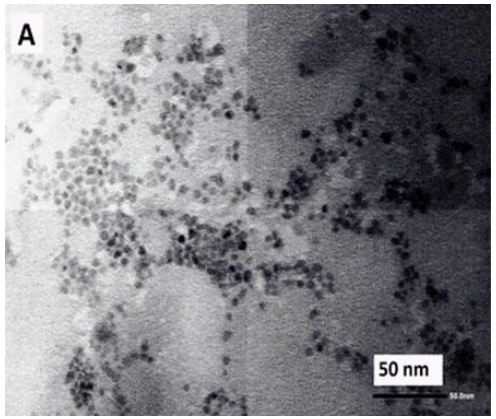
A
50 nm

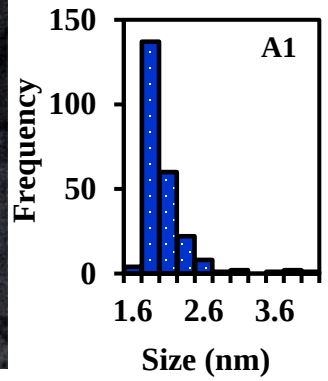
A1
Frequency
150
100
50
0
1.6
2.6
3.6
Size (nm)

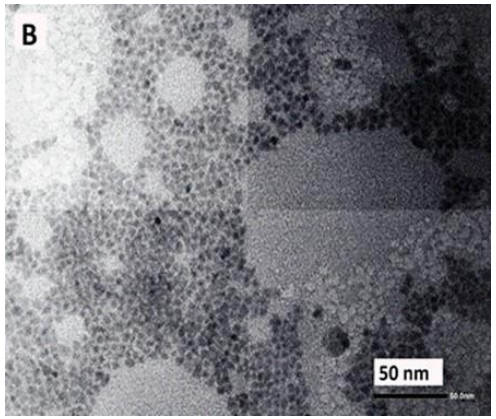
B
50 nm

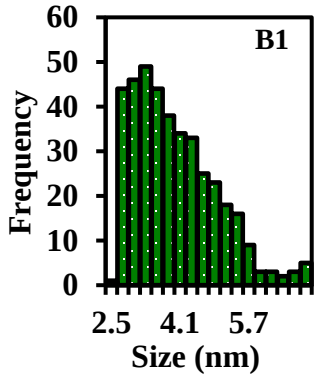
B1
Frequency
60
50
40
30
20
10
0
2.5
4.1
5.7
Size (nm)

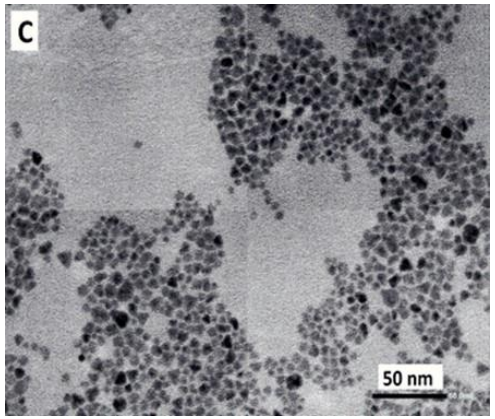
C
50 nm

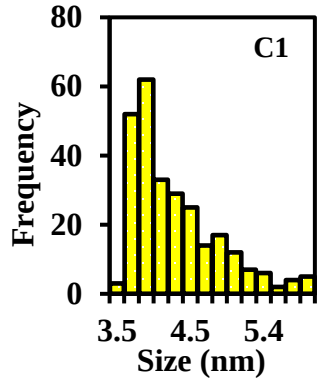
C1
Frequency
80
60
40
20
0
3.5
4.5
5.4
Size (nm)

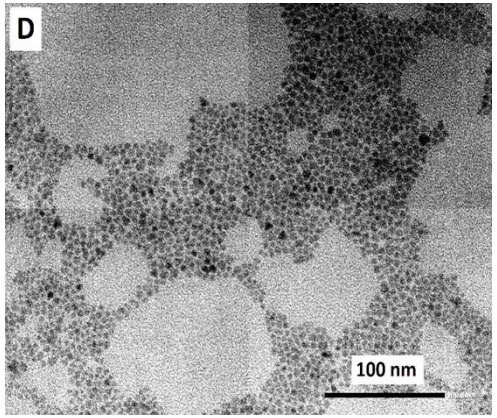
D
100 nm

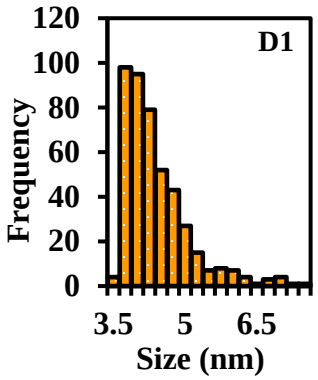
D1
Frequency
120
100
80
60
40
20
0
3.5
5
6.5
Size (nm)

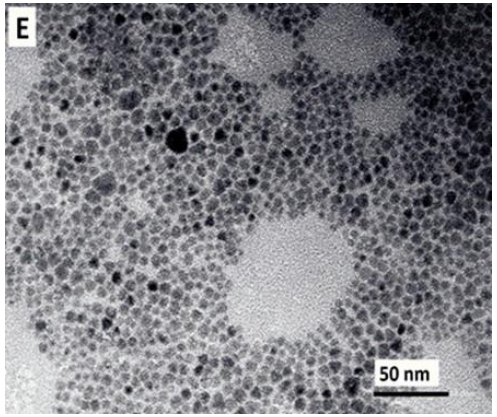
E
50 nm

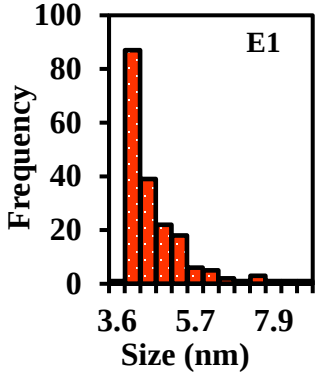
E1
Frequency
100
80
60
40
20
0
3.6
5.7
7.9
Size (nm)

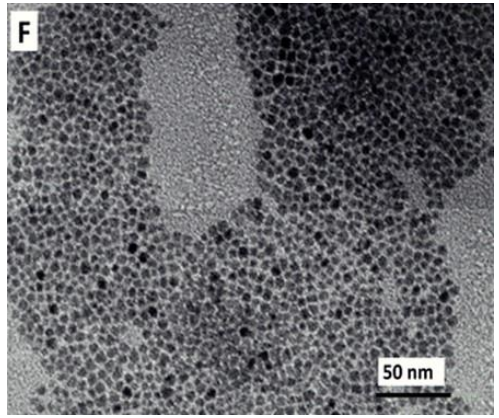
F
50 nm

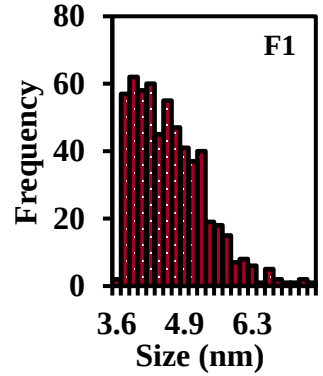
F1
Frequency
80
60
40
20
0
3.6
4.9
6.3
Size (nm)

Fig. 2, Adegoke and Park

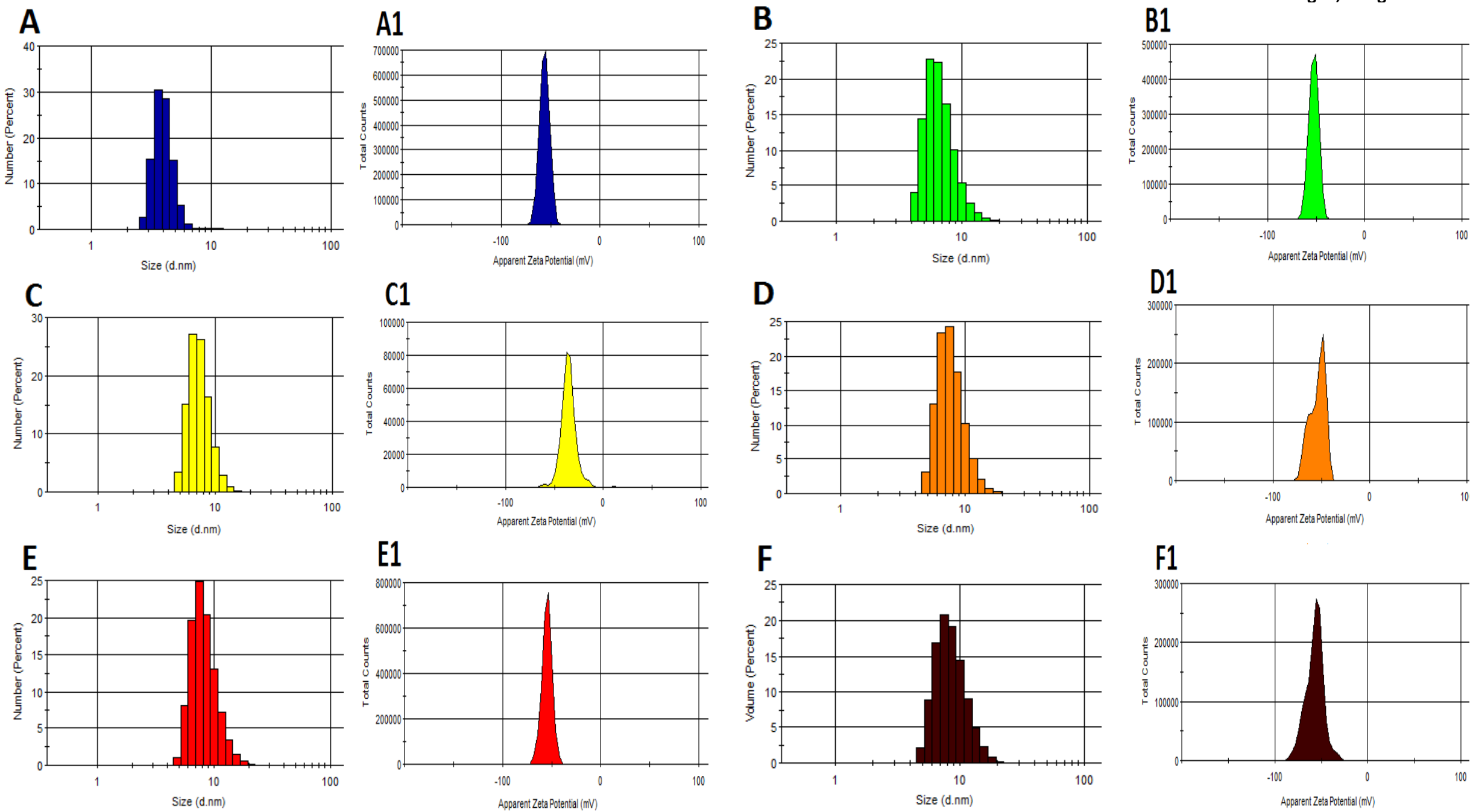

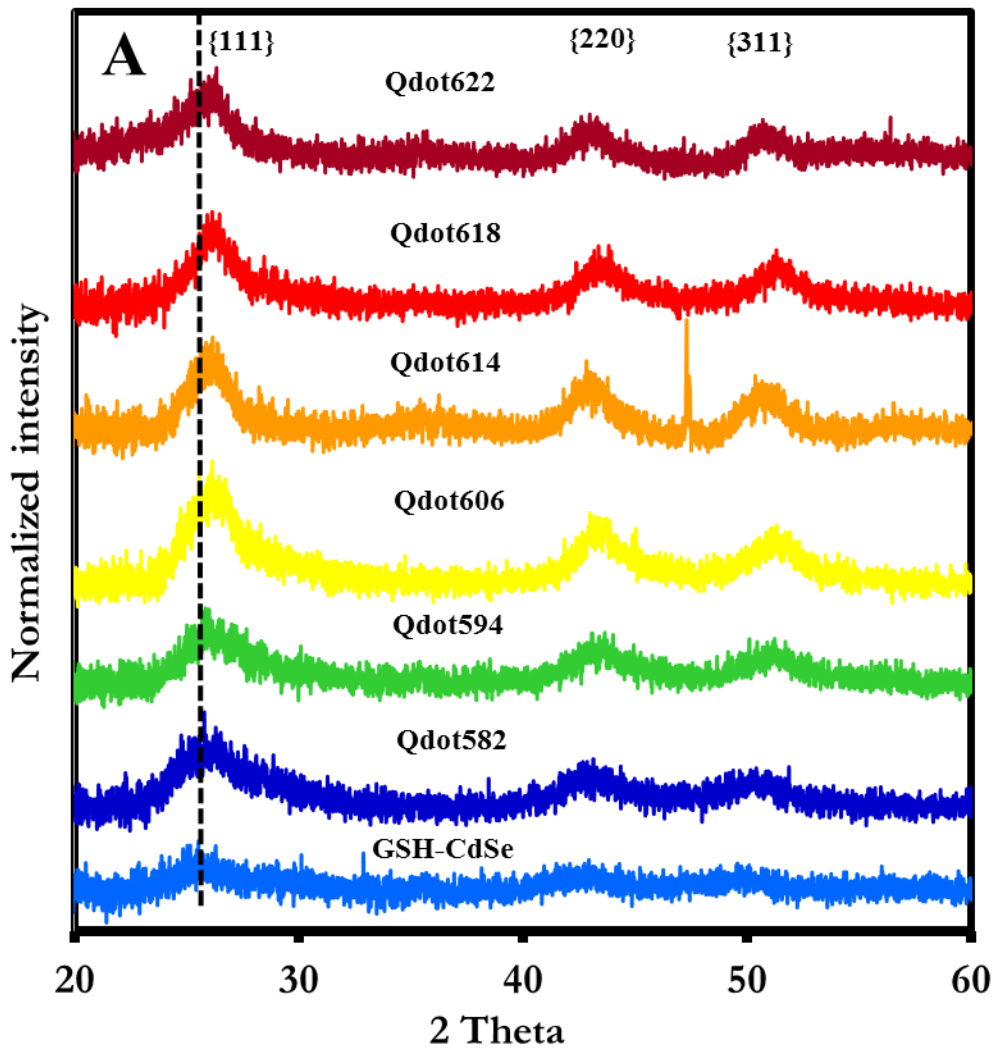

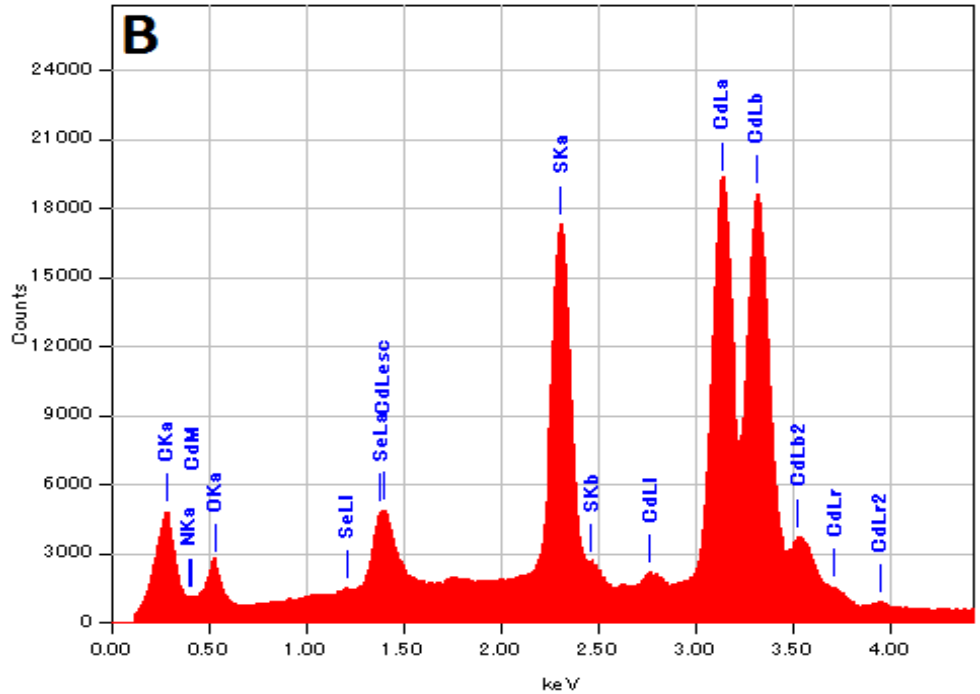

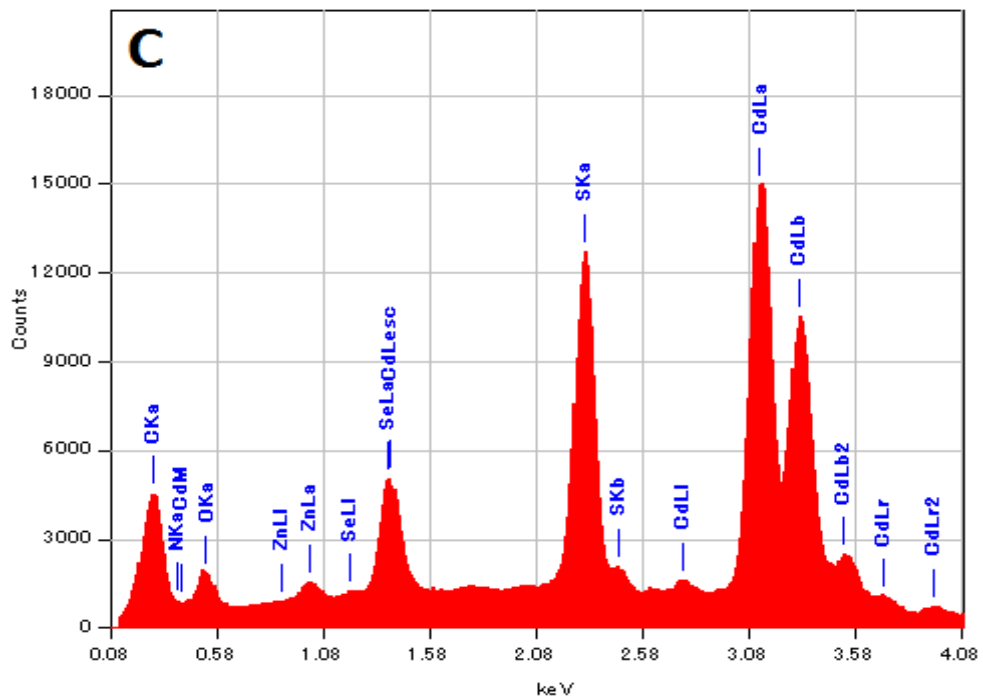

Fig. 3, Adegoke and Park

Fig. 4, Adegoke and Park

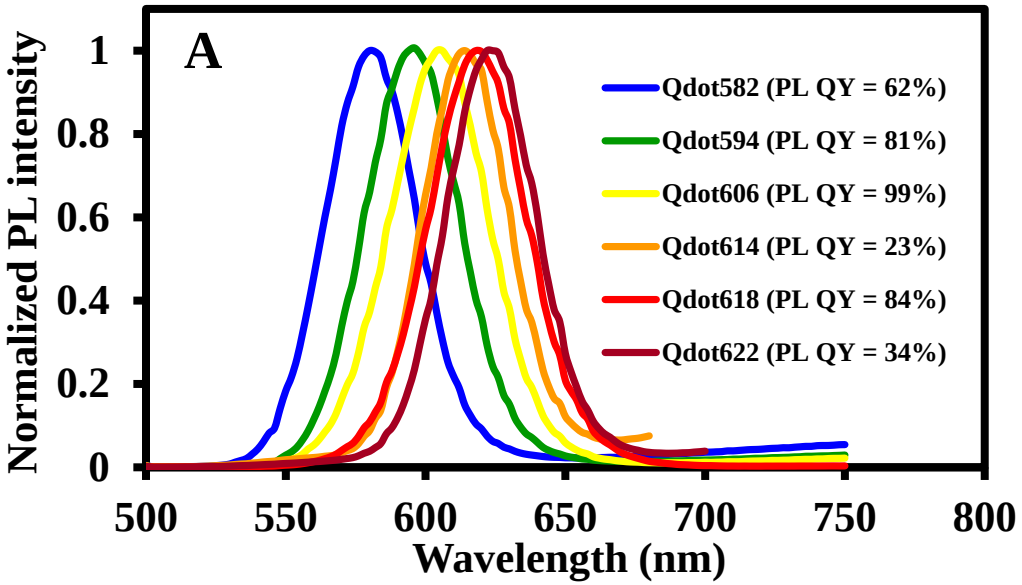

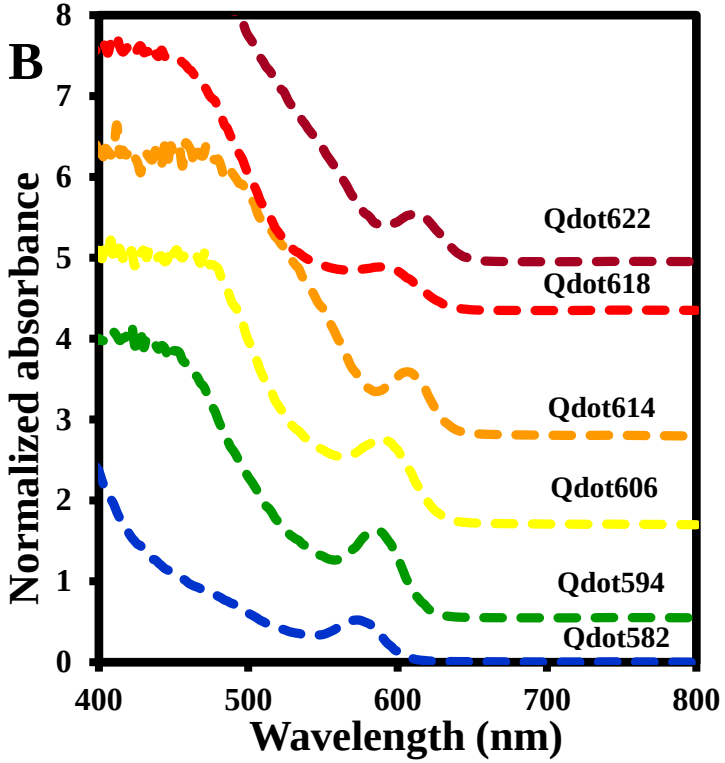

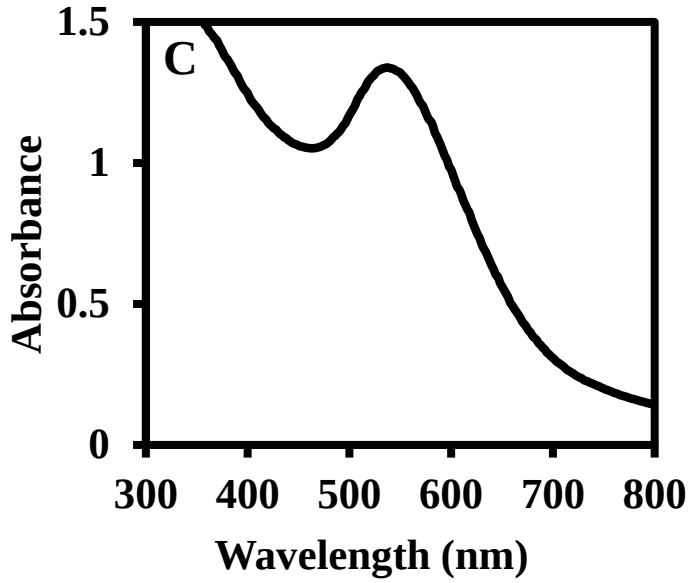

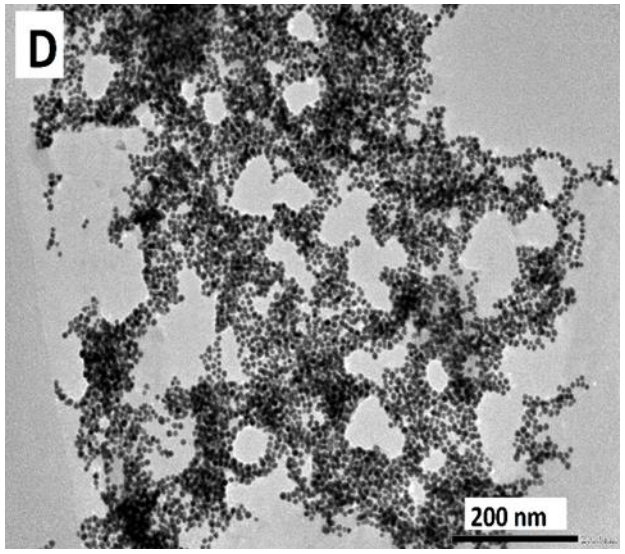

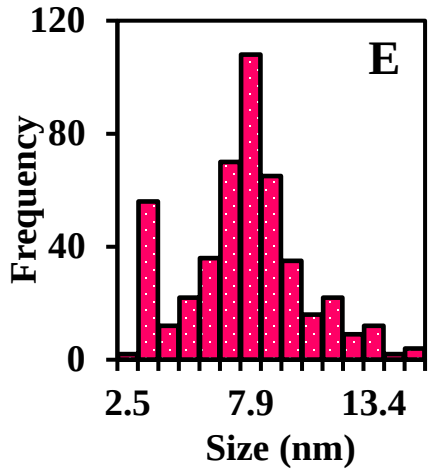

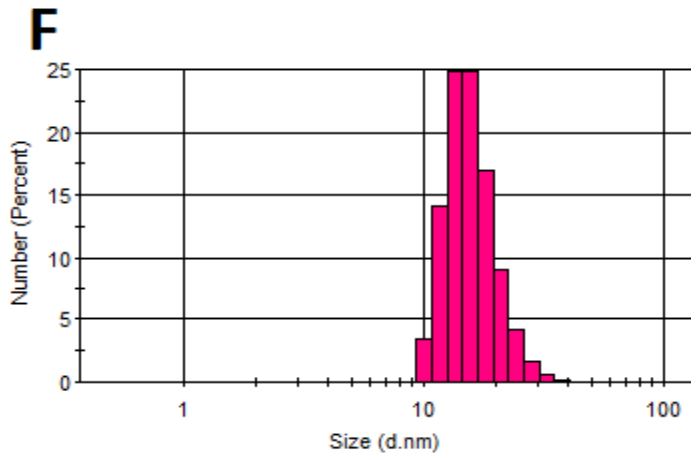

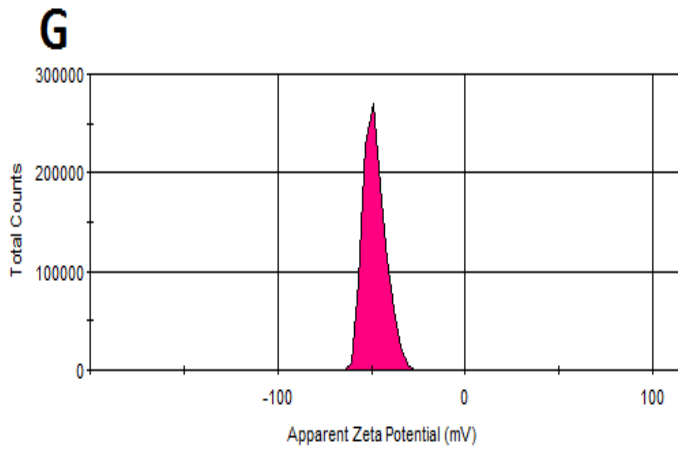

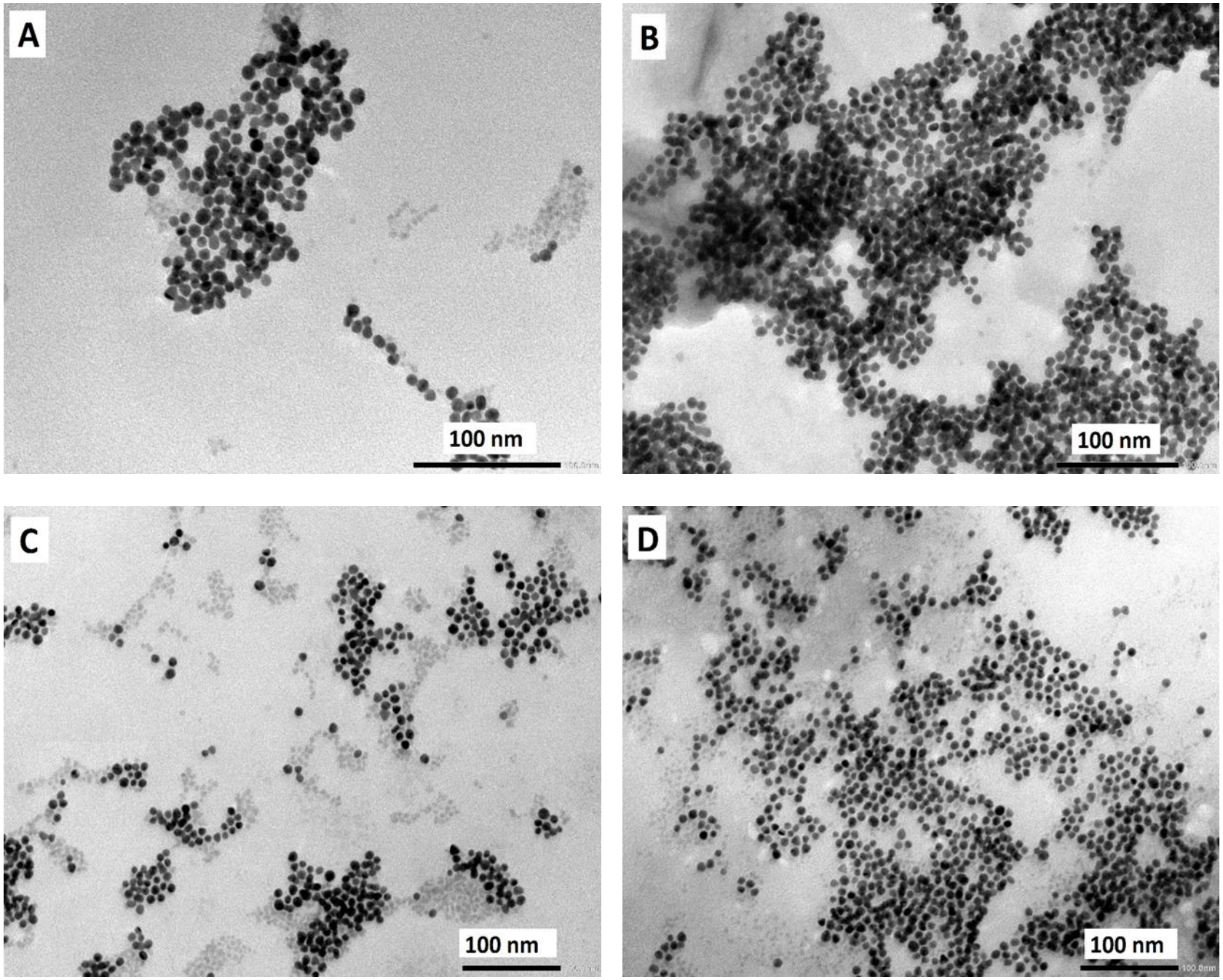
A
100 nm
B
100 nm
C
100 nm
D
100 nm

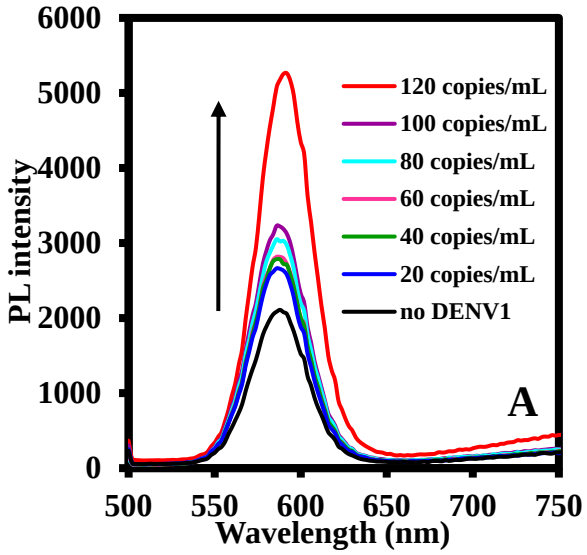
120 copies/mL
100 copies/mL
80 copies/mL
60 copies/mL
40 copies/mL
20 copies/mL
no DENV1
PL intensity
Wavelength (nm)
A

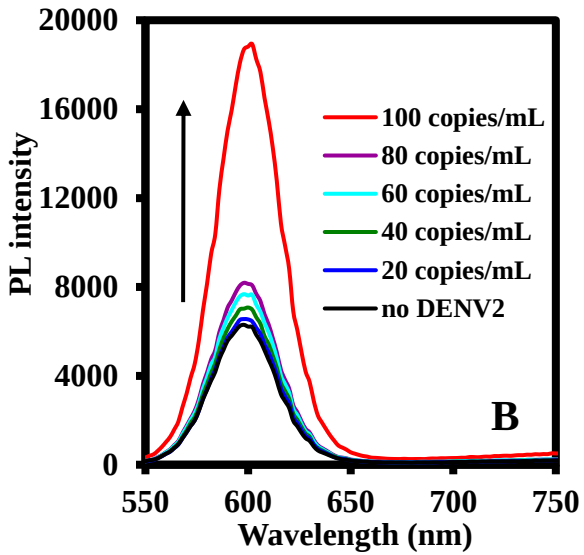
100 copies/mL
80 copies/mL
60 copies/mL
40 copies/mL
20 copies/mL
no DENV2
PL intensity
Wavelength (nm)
B

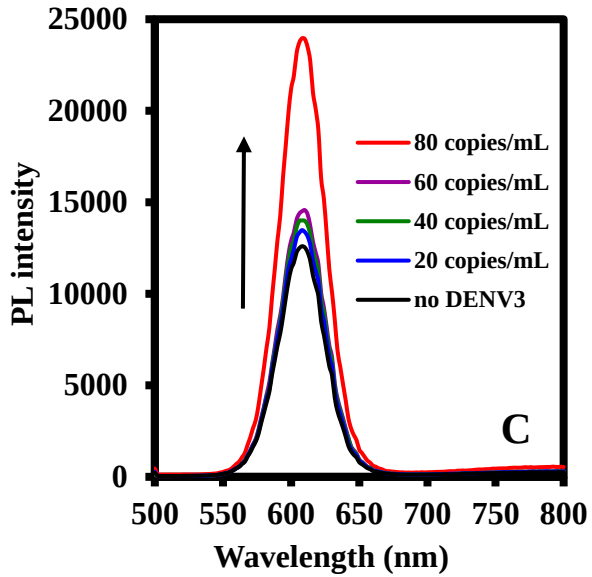
80 copies/mL
60 copies/mL
40 copies/mL
20 copies/mL
no DENV3
PL intensity
Wavelength (nm)
C

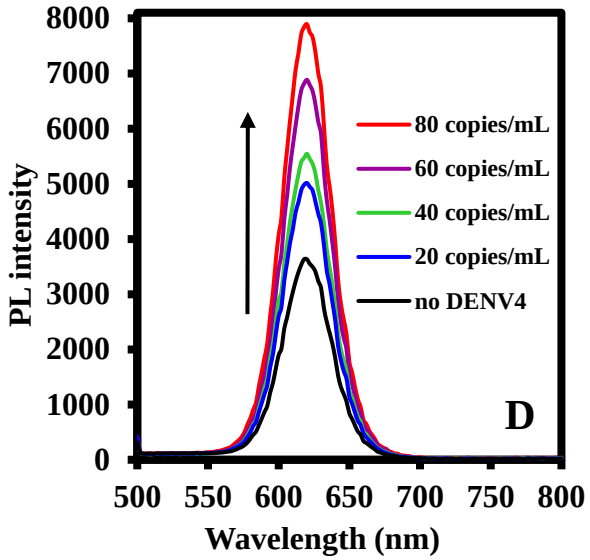
80 copies/mL
60 copies/mL
40 copies/mL
20 copies/mL
no DENV4
PL intensity
Wavelength (nm)
D

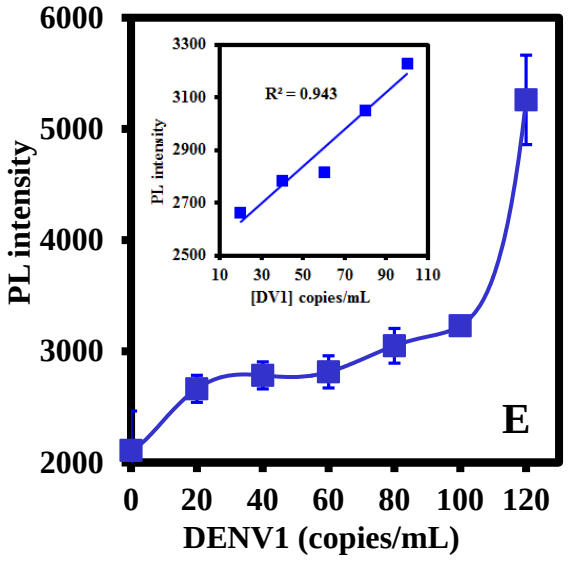
R² = 0.943
PL intensity
[DV1] copies/mL
DENV1 (copies/mL)
E

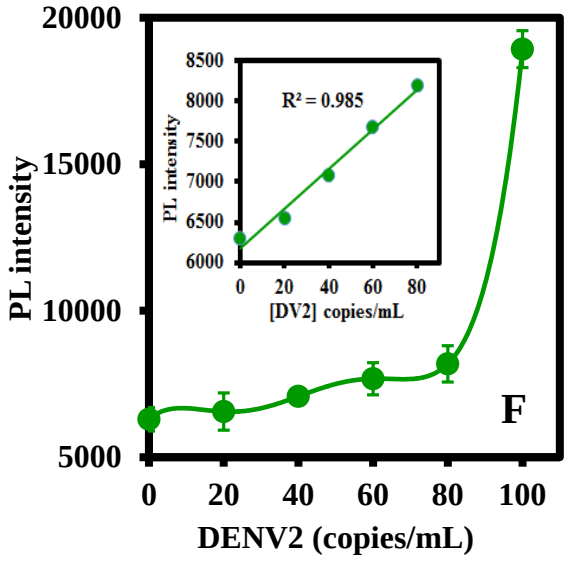
R² = 0.985
PL intensity
[DV2] copies/mL
DENV2 (copies/mL)
F

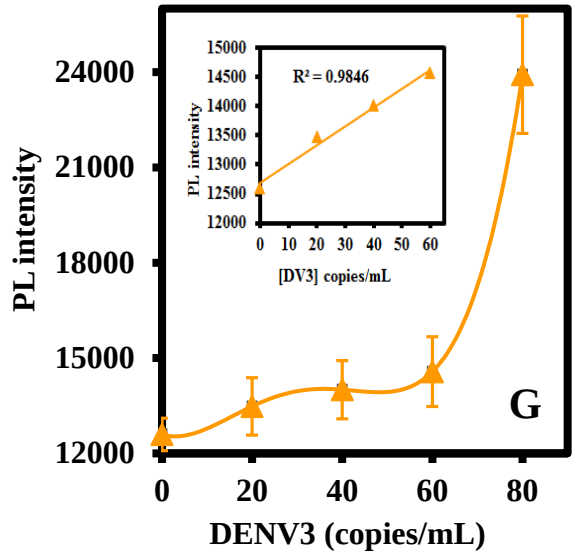
R² = 0.9846
PL intensity
[DV3] copies/mL
DENV3 (copies/mL)
G

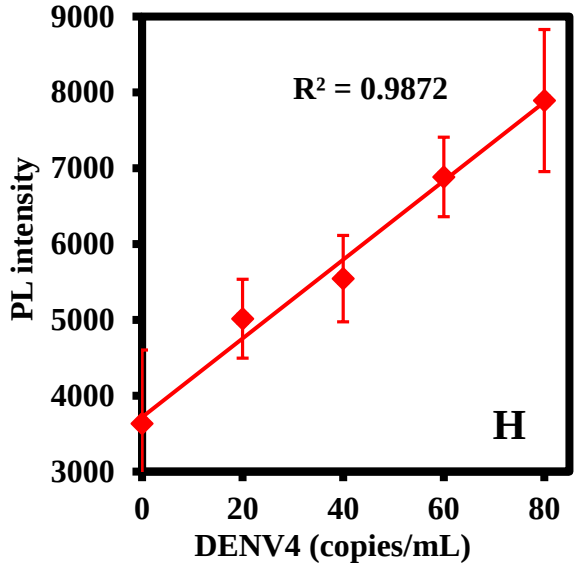
R² = 0.9872
PL intensity
DENV4 (copies/mL)
H

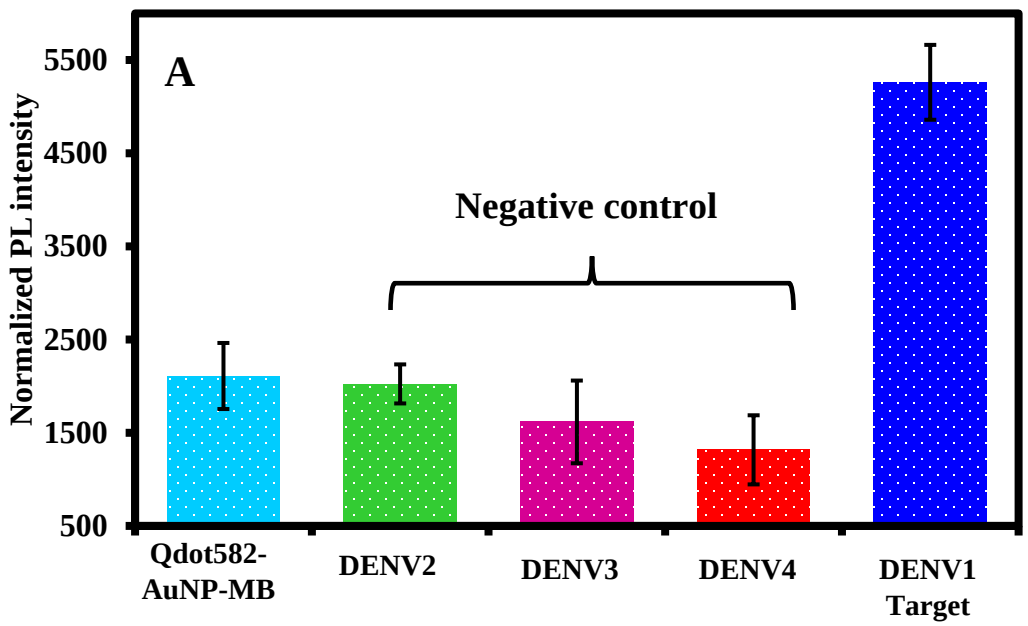
A
Normalized PL intensity
5500
4500
3500
2500
1500
500
Negative control
Qdot582-AuNP-MB
DENV2
DENV3
DENV4
DENV1 Target

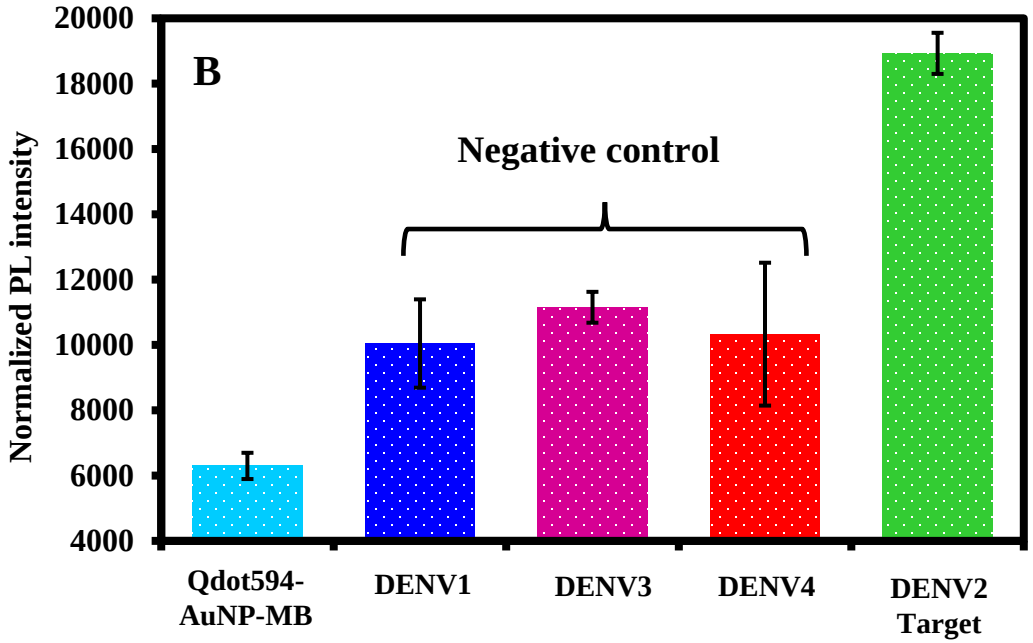
B
Normalized PL intensity
20000
18000
16000
14000
12000
10000
8000
6000
4000
Negative control
Qdot594-AuNP-MB
DENV1
DENV3
DENV4
DENV2 Target

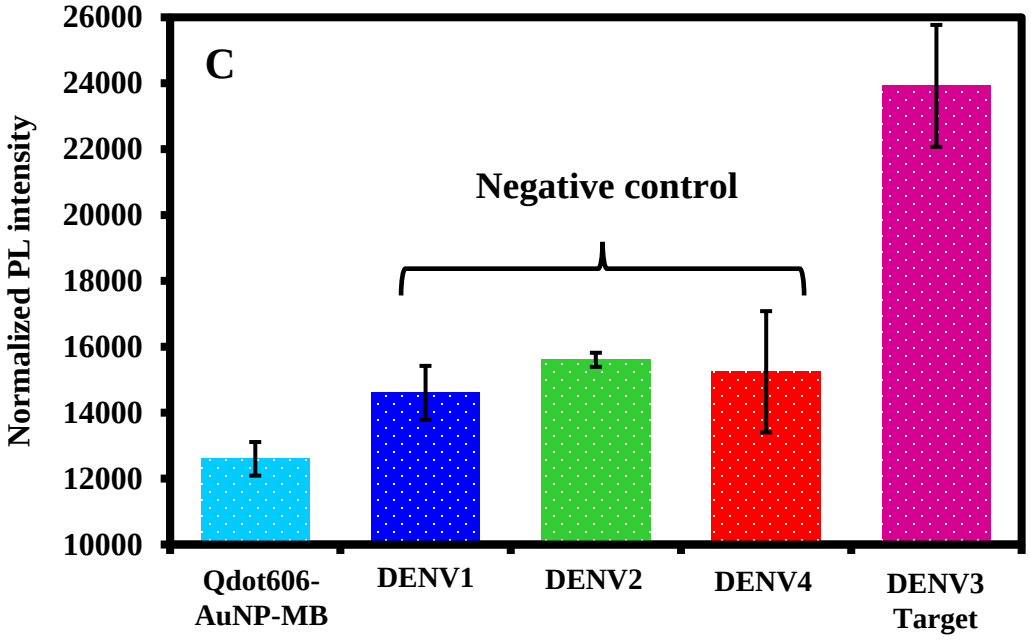
C
Normalized PL intensity
26000
24000
22000
20000
18000
16000
14000
12000
10000
Negative control
Qdot606-AuNP-MB
DENV1
DENV2
DENV4
DENV3 Target

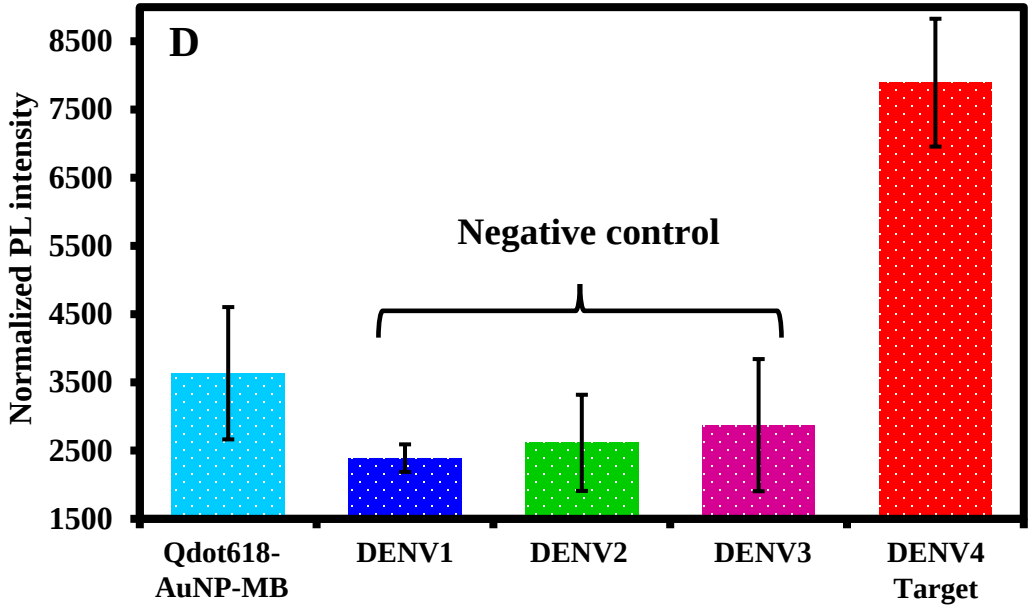
D
Normalized PL intensity
8500
7500
6500
5500
4500
3500
2500
1500
Negative control
Qdot618-AuNP-MB
DENV1
DENV2
DENV3
DENV4 Target

Supporting Information

Bright luminescent optically engineered core/alloyed shell quantum dots: An ultrasensitive signal transducer for dengue virus RNA via localized surface plasmon resonance-induced hairpin hybridization†

Oluwasesan Adegoke,[a] Enoch Y. Park[*,a,b]

[a] *Laboratory of Biotechnology, Research Institute of Green Science and Technology, Shizuoka University, 836 Ohya, Suruga-ku, Shizuoka 422-8529, Japan.*
E-mail: adegoke.sesan@mailbox.co.za , park.enoch@shizuoka.ac.jp

[b] *Laboratory of Biotechnology, Department of Bioscience, Graduate School of Science and Technology, Shizuoka University, 836 Ohya, Suruga-ku, Shizuoka 422-8529, Japan*

† Electronic supplementary information (ESI) available: MTT viability assay of Qdot606 to HEK 293T cells, PL lifetime decay curves of the Qdots, TEM images of the Qdot-AuNPs-MB biosensor conjugates, DLS and zeta potential of the Qdot-AuNP nanohybrids, DLS and zeta potential curves for the Qdot-AuNP-MB biosensor conjugate, fluorescence quenching effects of $_{L}$-cysteine AuNPs on the Qdots after conjugation and the fluorescence quenching effects of the MB on the Qdot-AuNP conjugates, fluorescence quenching effects of $_{L}$-cysteine AuNPs on the Qdots after conjugation and the fluorescence quenching effects of the MB on the Qdot-AuNP conjugates.

[*] Laboratory of Biotechnology, Research Institute of Green Science and Technology, Shizuoka University, 836 Ohya, Suruga-ku, Shizuoka 422-8529, Japan. E-mail: park.enoch@shizuoka.ac.jp

Cell viability assay

A cell viability experiment was carried out on the newly developed GSH-CdSe/ZnSeS core/alloyed shell Qdots using the methyl thiazol tetrazolium bromide (MTT) assay.[1] To each well of a 96-well plate, 100 µL cell suspension containing HEK 293T cells was seeded, resulting in a final density of 2 x 10^5 cells/mL. After incubation of the cells for 48 hr at 37°C, different concentrations of Qdot606 (used as a representative Qdot), from 0.01–0.1 mg/mL, were added to the wells. HEK 293T cells with no dots were used as the control. A 10 µL solution of MTT reagent (25 mg in 5 mL of PBS) was added to the cells containing Qdots after incubation for 24 hr. Afterward, the cells were incubated for an additional 4 hr, and 200 µL of PBS was added to each well. After removal of the media, 200 µL of DMSO was used to dissolve the formazan blue formed in the cell. A microplate reader was used to measure the absorbance of the cell assay at 530 nm. Triplicate measurements were carried out, and the average value was used.

Cell viability result

The toxicity of Qdots is a major concern for their widespread applications in biological systems. The coating of non-toxic shell layers is a strategic way to protect the Cd ion from leakage into the cell to render the Qdot non-toxic or with reduced toxicity. The cytotoxicity level of Cd-based chalcogenide Qdots is still debatable within the scientific community with varying theories of potential route for cell death.[2] In this work, we have carried out a simple MTT viability assay to probe the cytotoxicity of the newly synthesized GSH-CdSe/ZnSeS Qdots. Qdot606 was chosen as the representative Qdots for this analysis. The dose dependent (0.01 – 0.1 mg/mL) cell viability of Qdot606 to HEK 293T cells after 48 hr of exposure is shown in Fig. S-1. We found no apparent toxicity of the Qdots to the cells as the cell viability results show that no cell death occur. It is imperative to emphasize that the mg/mL dose level of Qdots used in this work is much higher than the µg/mL dose level usually reported in the

literature.[3-5] We can emphatically draw the conclusion that GSH-CdSe/ZnSeS Qdots exhibit excellent cell viability to HEK 293T cells.

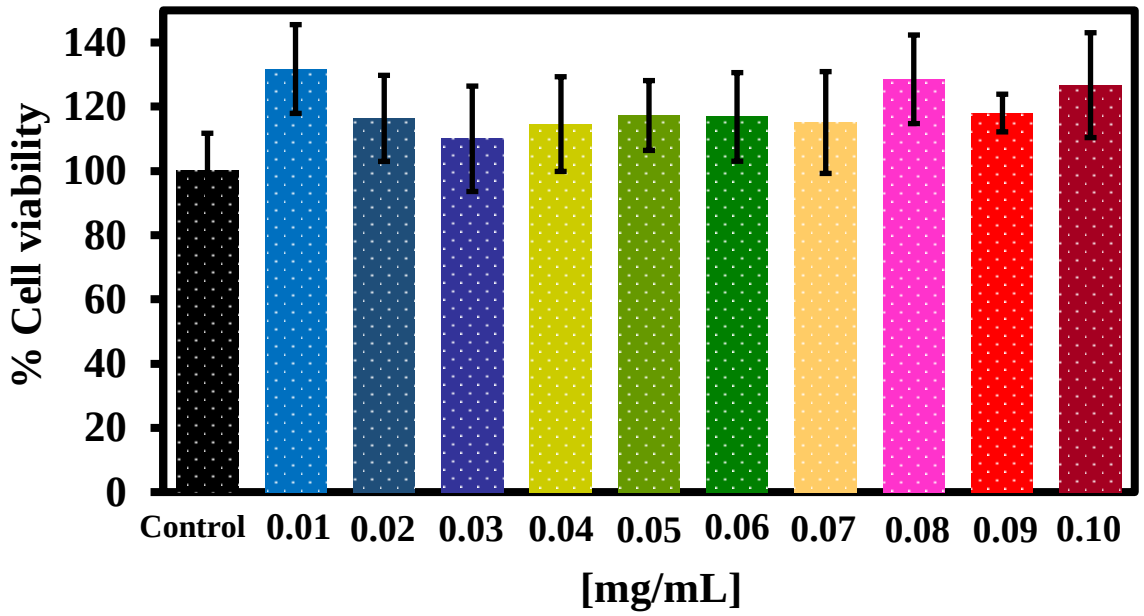

Fig. S-1. MTT viability assay of Qdot606 to HEK 293T cells.

PL Lifetime

Supplementary Fig. S-2 shows the single monoexponential PL decay curves for the size-dependent Qdots, and the PL lifetime value for each Qdot is indicated on each figure. Judging from the lifetime values, we can generally infer that no direct relationship exists between the Qdot size increase and PL QY for Qdot 614, Qdot618 or Qdot622. We believe that the single-dot monoexponential characteristic of the PL lifetime is induced by fluctuations that are directly aligned with single-dot emission intensities. These fluctuations in the radiative rate were not apparent for Qdot582, Qdot694 and Qdot606 because an increase in the particle size and PL QY was effectively correlated with an increase in the PL lifetime. If fluctuation in the radiative rate exists, a decline in the lifetime should correspond to an increase in the PL QY.[6] However, this was not the case, judging from the PL lifetime of Qdot614, Qdot618 and Qdot622. Surface defect states influenced by external trap sites generally lead to non-

radiative exciton relaxation pathways in single ensemble Qdots.[7] Therefore, the PL lifetime fluctuation reflects the coupling of the excited state of the Qdots to non-radiative exciton trap states.

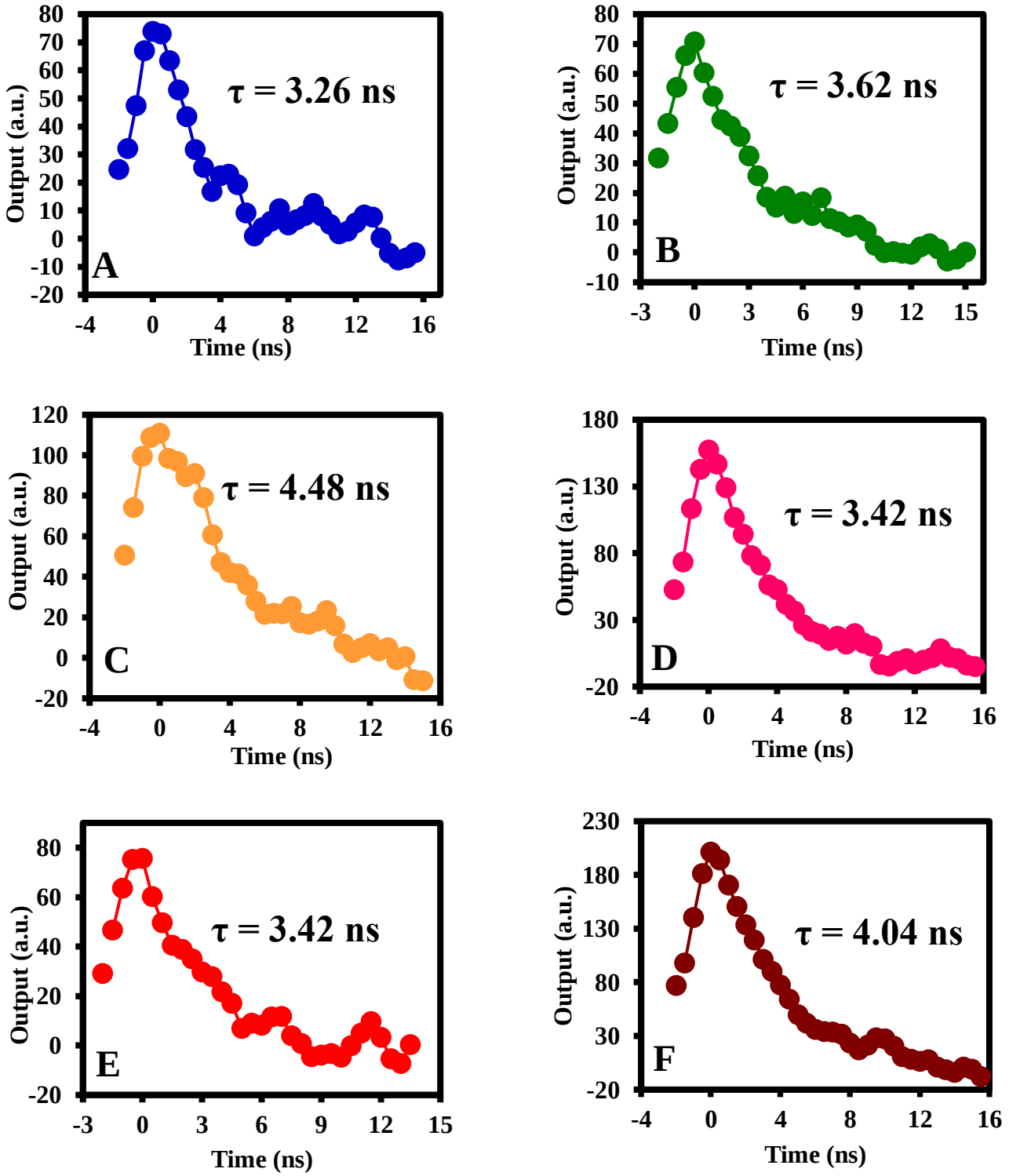

Fig. S-2. PL lifetime decay curves of (A) Qdot582, (B) Qdot594, (C) Qdot606, (D) Qdot614, (E) Qdot618 and (F) Qdot622.

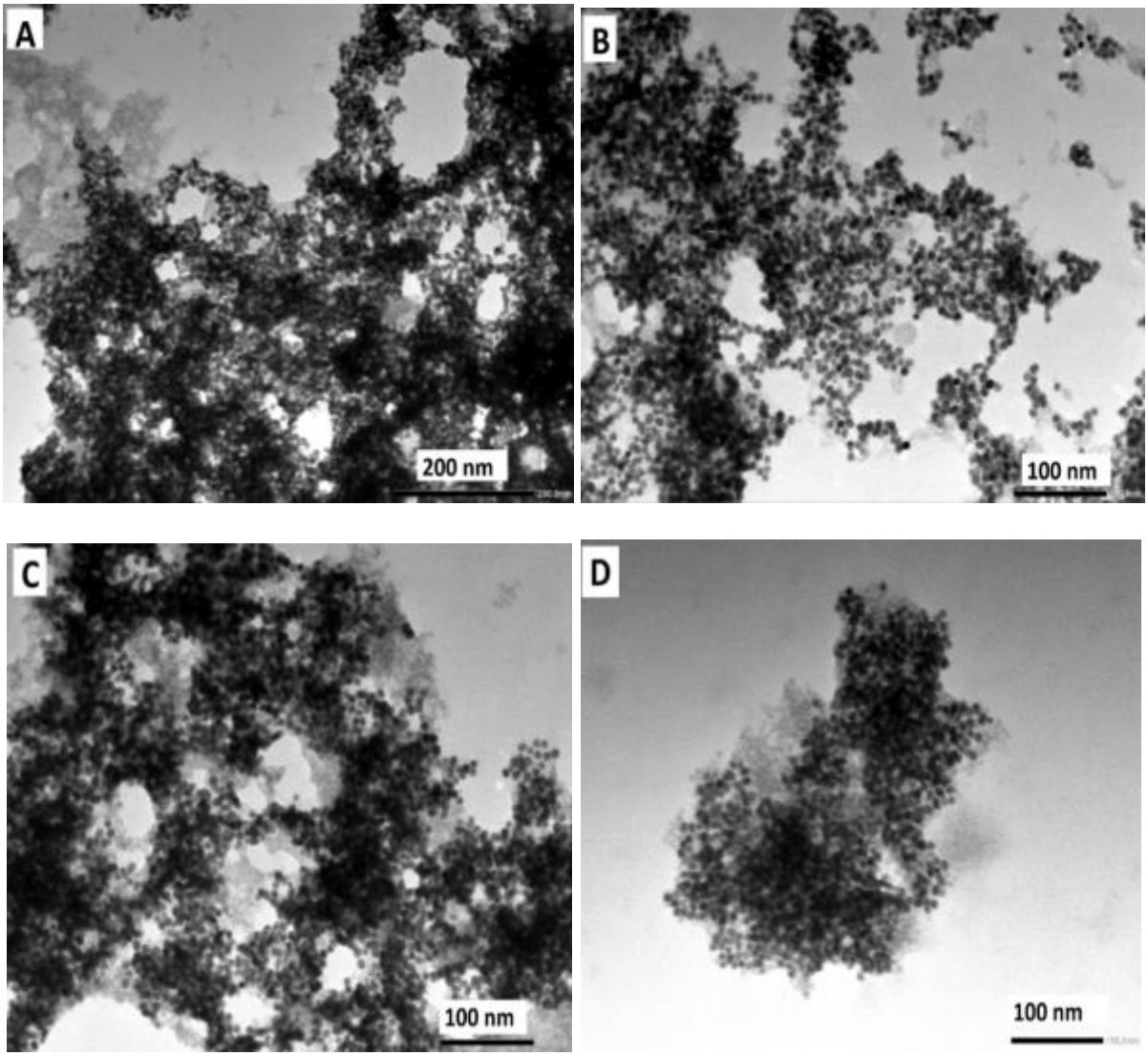

Fig. S-3. TEM images of (A) Qdot582-AuNPs-MB, (B) Qdot594-AuNPs-MB, (C) Qdot606-AuNPs-MB and (D) Qdot618-AuNPs-MB.

DLS and ZP of Qdot-AuNP conjugates

Fig. S-4A-D shows the DLS curves of the Qdot582-AuNP, Qdot594-AuNP, Qdot606-AuNP and Qdot618-AuNP conjugates. In this section, we utilize DLS as a technique to probe the aggregation state and dispersity of the conjugates. It is expected that the hydrodynamic size of the Qdot-AuNP conjugates should be higher than the size obtained for the individual Qdots and AuNPs. The values obtained are 87.7±21.6 nm for Qdot582-AuNPs, 57.5±21.0 nm for Qdot594-AuNPs, 69.1±38.8 nm for Qdot606-AuNPs and 52.3±21.5 nm for Qdot618-AuNPs. The values obtained indicate that the hydrodynamic particle size of the conjugates are still within the range of colloidal monodispersity. Although, the particles are more broadly distributed. This is expected due to the variability in the size distribution of the Qdots and AuNPs. The TEM images shown in Fig. 5 also confirms the monodispersity of the conjugates. Since the hydrodynamic size value of the conjugates are less than 100 nm, we can conclude that the conjugate solution are unagglomerated.

The corresponding ZP of the conjugates are shown in Fig. S-4A1-D1. ZP analysis was used to probe the colloidal stability of the conjugates. The values obtained are -40.9±4.2 mV for Qdot582-AuNPs, -41.2±4.4 mV for Qdot594-AuNPs, -39.0±4.3 mV for Qdot606-AuNPs and -42.5±5.0 mV for Qdot618-AuNPs. The ZP curves of the conjugates displayed high degree of stability as evident from the lack of peak splitting. The ZP values confirms that the colloidal solution of the conjugates are within the range of high colloidal stability. This imply that the strong binding of the Qdots to AuNPs did not distort the stability of the conjugate system, hence making them suitable for further conjugation to the MBs. Retaining the stability of nanoparticles within a conjugates system is challenging due to factors such as steric hindrance, aggregation and surface defects. Maintaining the stability of the conjugate system provides evidence that both the Qdots and AuNPs exhibit good optical properties.

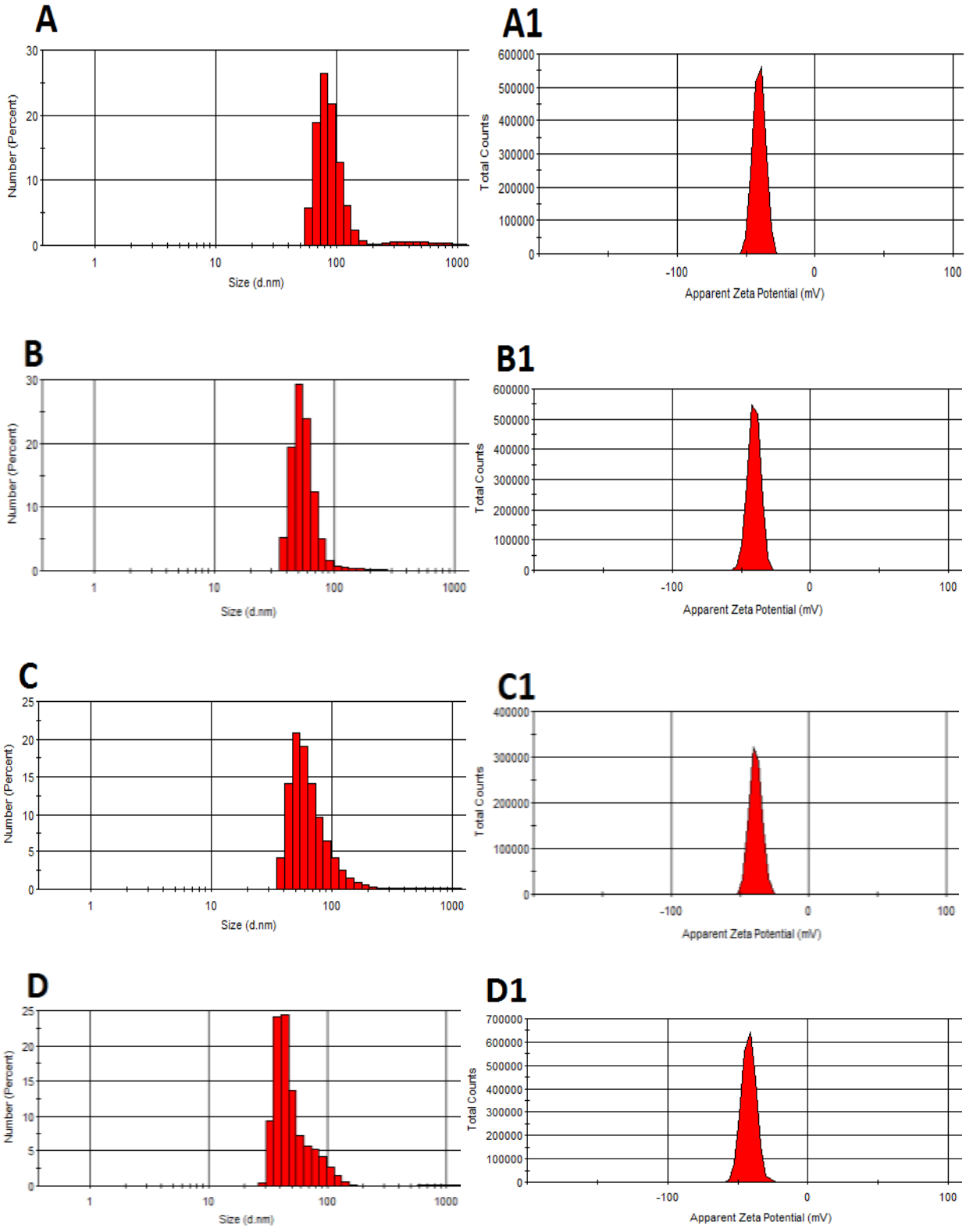

Fig. S-4. DLS (A-D) and zeta potential (A1-D1) curves for Qdot582-AuNP (A, A1), Qdot594-AuNP (B, B1), Qdot606-AuNP (C, C1) and Qdot618-AuNP (D, D1).

DLS and ZP of Qdot-AuNP-MB conjugates

The DLS plots of the Qdot-AuNP-MB conjugates are shown in Fig. S-5A-D. The ratio of Qdot-AuNPs to the MB was (2:0.5 v/v). As we have probed the monodispersity and aggregation state of the Qdot-AuNP conjugates in the previous section, we hereby perform similar assessment for the Qdot-AuNP-MB conjugates. The DLS values obtained are 126.9±23.2 nm for Qdot582-AuNP-MB, 74.4±27.2 nm for Qdot594-AuNP-MB, 102.4±22.4 nm for Qdot606-AuNP-MB and 96.9±19.8 nm for Qdot618-AuNP-MB. We directly observed an increase in the hydrodynamic particle size in comparison to the Qdot-AuNP conjugates. The increase is due to the strong binding of the Qdot-AuNP conjugates to the MB. With the exception of Qdot594-AuNP-MB and Qdot618-AuNP-MB, the hydrodynamic particle size of Qdot582-AuNP-MB and Qdot606-AuNP-MB are greater than 100 nm. This values obtained are not surprising but expected due to the coarseness in the particle distribution following the strong binding to the MB.

Fig. S-5A1-D1 shows the corresponding ZP plots for the Qdot-AuNP-MB conjugates. The emphasis here is to probe the colloidal stability of the resulting Qdot-AuNP-MB conjugates as we have performed above for the Qdot-AuNP conjugates. The values obtained are -34.8±3.6 mV for Qdot582-AuNPs-MB, -36.6±7.5 mV for Qdot594-AuNPs-MB, -35.6±4.1 mV for Qdot606-AuNPs-MB and -36.6±5.5 mV for Qdot618-AuNPs-MB. It is quite surprising that after the strong binding of the plasmonic fluorophore to the MB, the ZP of the resulting conjugates are still within the range of high colloidal stability. We attribute the strong stability of the conjugates to the spectacular optical properties of the Qdots and AuNPs.

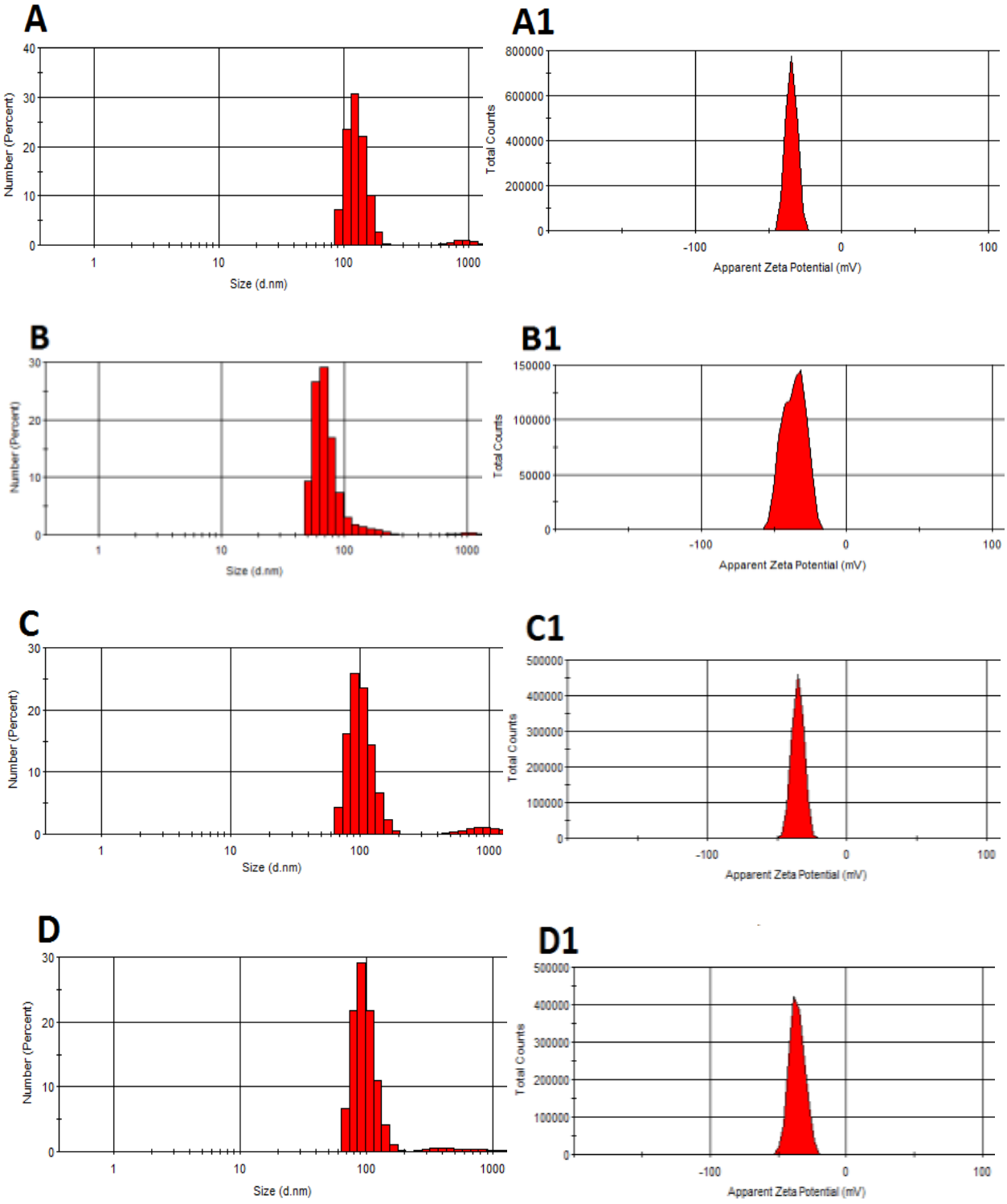

Fig. S-5. DLS (A-D) and zeta potential (A1-D1) curves for Qdot582-AuNP-MB (A, A1), Qdot594-AuNP-MB (B, B1), Qdot606-AuNP-MB (C, C1) and Qdot618-AuNP-MB (D, D1) biosensor conjugate probes.

PL Quenching effects after conjugation

Fig. S6A-D shows the fluorescence quenching effect of Qdot-AuNP and Qdot-AuNP-MB conjugates. After conjugation of AuNPs to the Qdots, the strong binding effect which could arise from energy transfer from the Qdots to AuNP induces the fluorescence of the Qdots to be quenched. The quenching effects of the MBs on the fluorescence of the Qdot-AuNP conjugate are also shown.

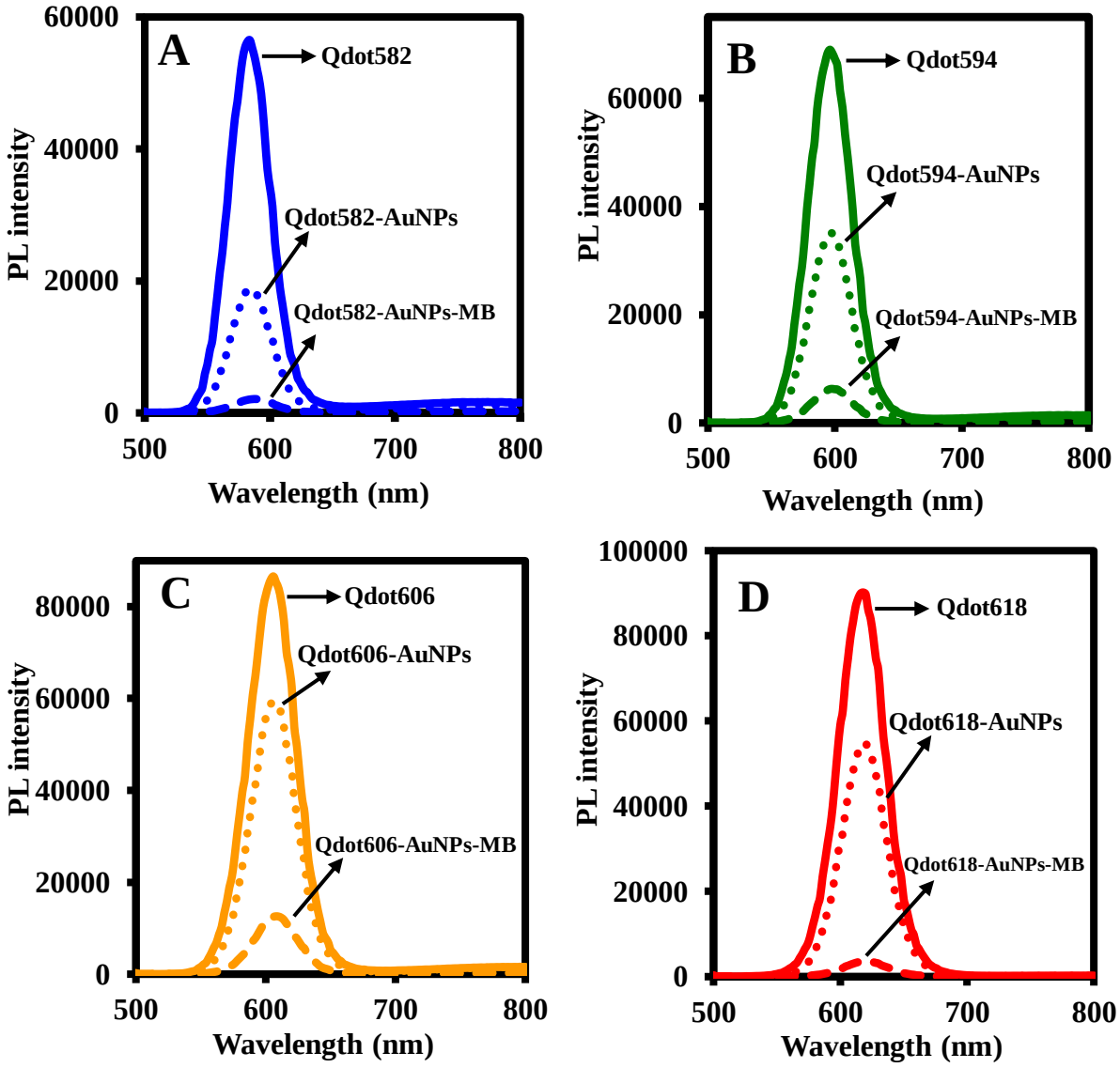

Fig. S-6. Fluorescence quenching effects of L-cysteine AuNPs on the Qdots after conjugation and the fluorescence quenching effects of the MB on the Qdot-AuNP conjugates.

In this section, we discuss the comparison in detection sensitivity of the Qdot-AuNP-MB biosensor probe with the Qdot-MB probe (having no influence of LSPR signal from AuNPs). The highest concentration of DENV detected by the Qdot-AuNP-MB biosensor probe was used for comparison. Fig. S-7A-D shows the comparison in PL intensity of the Qdot-AuNP-MB and Qdot-MB probes before and after detection of the target DENV. Our analysis shows that LSPR signal from AuNPs enhanced the sensitivity of the biosensor probe, hence making the Qdot-AuNP-MB a more superior biosensor probe.

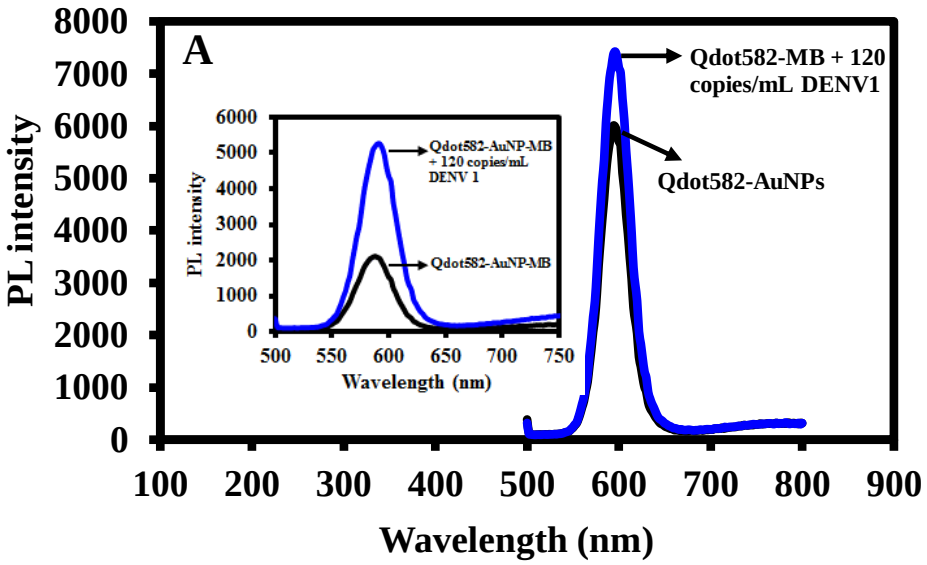

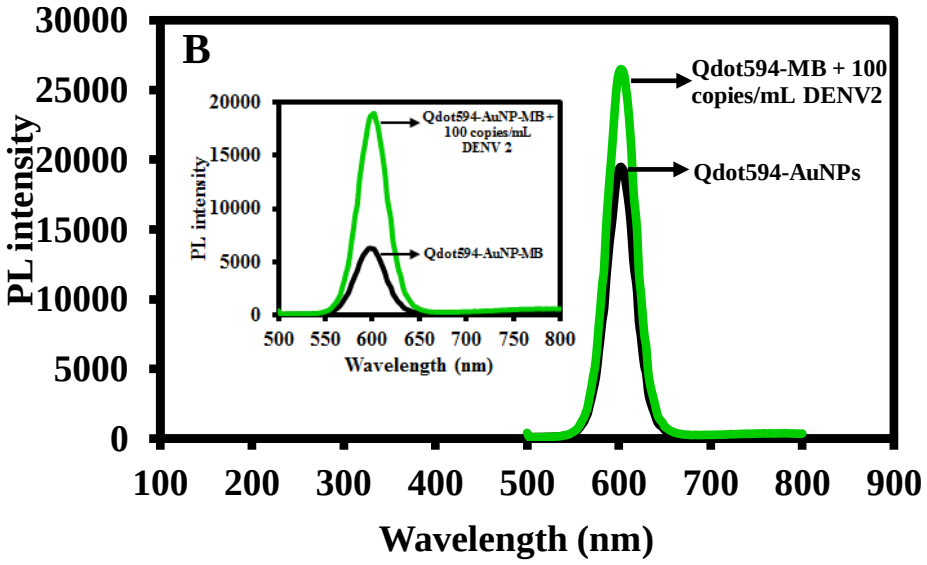

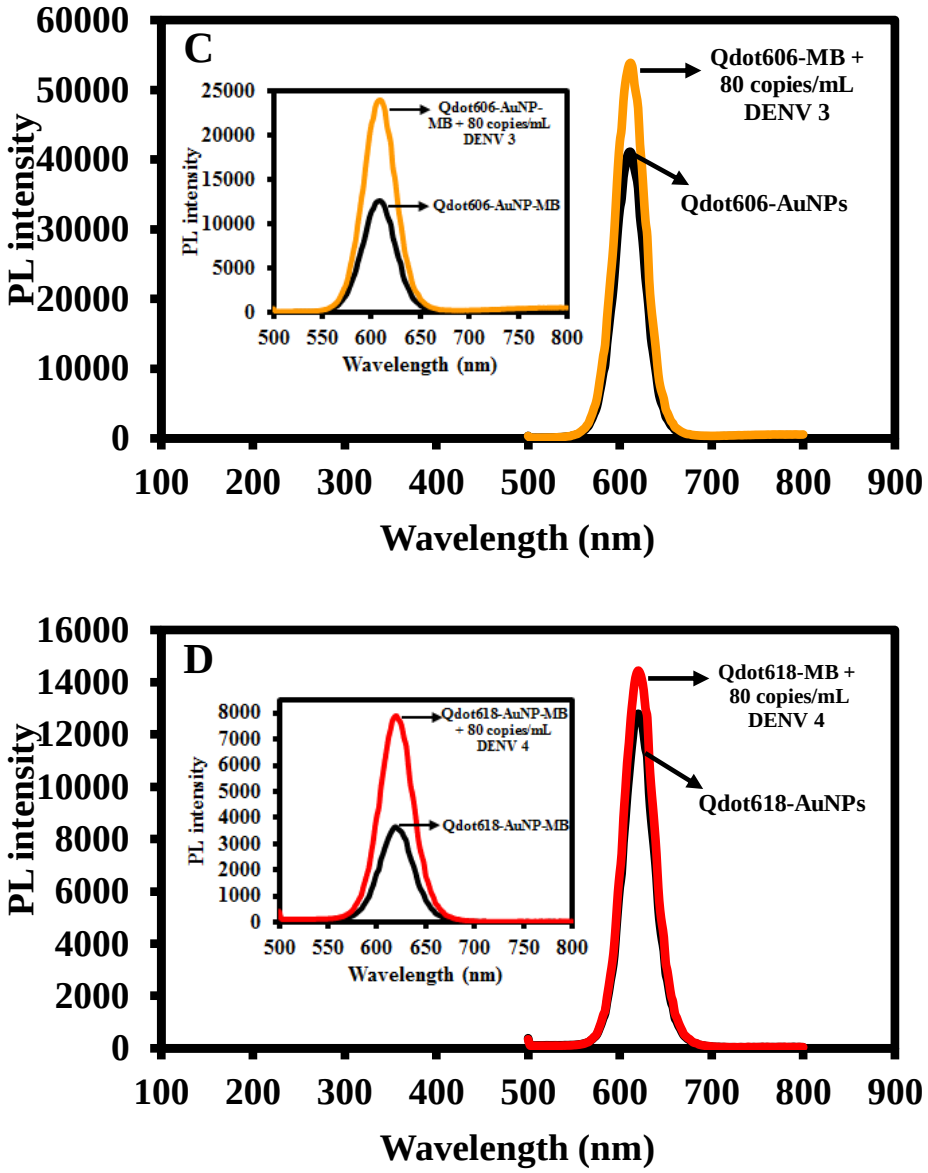

Fig. S-7. Comparison of the PL switch on detection of DENV1-4 using the Qdots-MB probe and the Qdot-AuNP-MB biosensor probe (inset). Detection of (A) 120 copies/mL DENV1, (B) 120 copies/mL DENV2, (C) 80 copies/mL DENV3 and (D) 80 copies/mL DENV4.

References

1. T. Mosmann, *J. Immunol. Methods*, 1983, **65**, 55–63.
2. R. A. Hardman, *Environ. Health Perspect.*, 2006, **114**, 165–172.
3. J. Liu, R. Hu, J. Liu, B. Zhang, Y. Wang, X. Liu, W. C. Law, L. Liu, L. Ye, K. T. Yong, *Mat. Sci. Eng. C-Mater.*, 2015, **57**, 222–231.
4. M. S. Stan, I. Memet, C, Sima, T. Popescu, V. S. Teodorescu, A. Hermenean, A. *Chem. Biol. Interact.*, 2014, **220**, 102–115.
5. M. Yan, Y. Zhang, H. Qin, K. Liu, M. Guo, Y. Ge, M. Xu, Y. Sun, X. Zheng, *Int. J. Nanomed.*, 2016, **11**, 529–542.
6. M. G. Bawendi, P. J. Carroll, W. L. Wilson, L. E. Brus, *J. Chem. Phys.*, 1992, **96**, 946–954.
7. O. Adegoke, M.-W. Seo, T. Kato, S. Kawahito, E. Y. Park, J. Mater. Chem B, 2016, **4**, 1489–1498.